AGU ADVANCING EARTH AND SPACE SCIENCES

JGR Atmospheres

RESEARCH ARTICLE
10.1029/2025JD045837

Improving FY-4A/AGRI BT Simulations Over Rugged Areas via Enhanced Solar Radiative Effects in WRF

Yang Wu[1,2], Xin Li[1,2], Anning Huang[3], Chunlei Gu[3], and Shuxin Cai[4]

[1]Nanjing Innovation Institute for Atmospheric Sciences, Chinese Academy of Meteorological Sciences-Jiangsu Meteorological Service, Nanjing, China, [2]Jiangsu Key Laboratory of Severe Storm Disaster Risk / Key Laboratory of Transportation Meteorology of CMA, Nanjing, China, [3]School of Atmospheric Sciences, Nanjing University, Nanjing, China, [4]Zhejiang Meteorological Service Center, Hangzhou, China

Key Points:

- Modeled land surface temperature (LST) errors cause biases in simulating surface-sensitive infrared brightness temperature over rugged areas
- A sub-grid terrain solar radiative effect scheme in WRF reduces terrain-related daytime overestimation in solar radiation and clear-sky LST
- Improved background clear-sky LST mitigates terrain-induced modeling biases in FY-4A/Advanced Geosynchronous Radiation Imager surface-sensitive infrared brightness temperature

Correspondence to:

X. Li and A. Huang,
lixinkimi@cma.gov.cn;
anhuang@nju.edu.cn

Citation:

Wu, Y., Li, X., Huang, A., Gu, C., & Cai, S. (2026). Improving FY-4A/AGRI BT simulations over rugged areas via enhanced solar radiative effects in WRF. *Journal of Geophysical Research: Atmospheres*, *131*, e2025JD045837. https://doi.org/10.1029/2025JD045837

Received 9 NOV 2025
Accepted 26 MAR 2026

Author Contributions:

Conceptualization: Yang Wu, Xin Li, Anning Huang
Data curation: Yang Wu, Xin Li
Formal analysis: Yang Wu, Xin Li, Anning Huang, Chunlei Gu, Shuxin Cai
Funding acquisition: Xin Li, Anning Huang
Investigation: Yang Wu, Xin Li, Anning Huang
Methodology: Yang Wu, Xin Li, Anning Huang
Software: Yang Wu, Xin Li, Anning Huang
Supervision: Yang Wu, Xin Li, Anning Huang
Validation: Yang Wu, Xin Li, Anning Huang
Visualization: Yang Wu, Xin Li, Anning Huang
Writing – original draft: Yang Wu, Xin Li, Anning Huang
Writing – review & editing: Yang Wu, Xin Li, Anning Huang, Chunlei Gu, Shuxin Cai

Abstract

Effective assimilation of satellite land surface-sensitive infrared brightness temperature (BT) depends critically on accurate background land surface temperature (LST), which is closely linked to surface downward solar radiation ($SW_{\downarrow}$) simulations. However, current numerical models often neglect topographic effects on $SW_{\downarrow}$, producing significant biases over rugged terrain and consequently degrading modeled LST. This study aims to improve FY-4A/Advanced Geosynchronous Radiation Imager clear-sky surface-sensitive infrared BT simulations by enhancing the representation of $SW_{\downarrow}$ and LST over mountainous regions. To this end, a three-dimensional sub-grid terrain solar radiative effect scheme (3DSTSRE) is incorporated into the Weather Research and Forecasting model. The analysis focuses on areas spanning the southeastern Tibetan Plateau and Sichuan Basin. Results show that 3DSTSRE substantially mitigates terrain-dependent $SW_{\downarrow}$ overestimation, decreasing regional-mean bias by 76.86% from 22.08 to 5.11 Wm^{-2}, with larger improvements over rugged terrain with sky view factor (SVF) less than 0.90. Correspondingly, clear-sky LST overestimation is effectively alleviated, with the bias reduced by 61.18% (1.70°C–0.66°C) over SVF $\leq$ 0.90 regions. These improvements occur primarily during daytime hours (08:00–18:00 Beijing Time). Consequently, terrain-dependent clear-sky BT overestimations for FY-4A/AGRI channels 11–13 are markedly reduced. Over rugged terrain, the daytime negative BT observation-minus-background biases decrease by 60.53%, 54.96%, and 51.26%, from −1.14, −1.31, and −1.19 K to −0.45, −0.59, and −0.58 K, respectively. The findings highlight the value of incorporating 3DSTSRE into numerical models to improve $SW_{\downarrow}$ and LST simulations, thereby reducing terrain-induced BT biases and benefiting the assimilation of surface-sensitive infrared observations over rugged terrain.

Plain Language Summary

Accurate simulation of FY-4A/AGRI surface-sensitive infrared brightness temperatures (BT) over land is essential for improving satellite data assimilation and analyses of near-surface atmospheric thermodynamic states. However, current BT simulations exhibit substantial biases, particularly in mountainous regions. These BT biases are closely related to errors in background land surface temperature (LST), which largely result from inadequate representation of topographic effects on surface downward solar radiation ($SW_{\downarrow}$). To address this issue, we incorporate a three-dimensional sub-grid terrain solar radiative effect (3DSTSRE) scheme into the Weather Research and Forecasting model. This scheme provides a more realistic representation of terrain-modulated solar radiation distribution, thereby enhancing both $SW_{\downarrow}$ and LST simulations over rugged terrain. Results show that including 3DSTSRE significantly reduces $SW_{\downarrow}$ overestimation, particularly in highly rugged terrain such as the southeastern Tibetan Plateau and Sichuan Basin. This correction leads to notable improvements in terrain-dependent clear-sky LST biases during the daytime. Consequently, negative biases in FY-4A/AGRI clear-sky surface-sensitive infrared BT simulations are markedly reduced. These findings underscore the importance of incorporating 3DSTSRE into numerical models to enhance $SW_{\downarrow}$ and LST simulations, thereby benefiting the assimilation and application of surface-sensitive infrared satellite data in mountainous regions.

1. Introduction

In recent decades, advancements in satellite remote sensing technology have greatly enhanced our ability to observe the Earth's atmosphere, oceans, and land. The new generation of geostationary satellites, for example, American Geostationary Operational Environmental Satellites (Schmit et al., 2005, 2017), Japanese Himawari-8/9 (Bessho et al., 2016), European Meteosat Third Generation (Ouaknine et al., 2013), and the Chinese Fengyun-

4A/B (FY-4A/B, Yang et al., 2017), are equipped with advanced imagers that provide high spatiotemporal resolution observations for specific regions. These satellites play a critical role in retrieving meteorological variables from the surface to the upper atmosphere, monitoring and nowcasting fast-evolving hazardous weather systems, and improving numerical weather prediction (NWP) through data assimilation (Gravelle et al., 2016; Kazumori, 2018; Minamide & Zhang, 2017; Ma et al., 2017; Okamoto et al., 2023; Xu et al., 2023; Zou et al., 2011).

Satellite data over oceans have been widely assimilated into NWP systems. However, over land, large brightness temperature (BT) observation-minus-background (OMB) biases remain, mainly due to difficulties in accurately estimating land surface temperature (LST) and emissivity (LSE). As a result, surface-sensitive infrared channels, which contain valuable near-surface thermodynamic information, are often excluded from data assimilation (English, 2008; Trigo et al., 2015; Zhuge et al., 2018). Recent advances have facilitated better utilization of surface-sensitive channels. These include the development of high-accuracy, dynamically varying emissivity atlases tailored to different wavelengths and surface types (Borbas & Ruston, 2010; Hulley et al., 2015; Vogel et al., 2011), the integration of ground-based or satellite retrieved observations combined with variational analysis for improved land surface parameter estimates (Guedj et al., 2011; Li et al., 2023, Li, Zou, et al., 2024; Pavelin & Candy, 2014), and enhancements in land surface modeling that refine LST forecasts in NWP background fields (Zheng et al., 2012). So far, the assimilation of surface-sensitive observations from instruments such as the Infrared Atmospheric Sounding Interferometer (Cayla, 2001), Atmospheric Infrared Sounder (AIRS, Chahine et al., 2006), and Spinning Enhanced Visible and Infrared Imager (SEVIRI, Schmetz et al., 2002) has shown promising results. These observations have been demonstrated to significantly improve lower-tropospheric temperature and mid-tropospheric humidity analyses, thereby enhancing both regional and global weather forecasting skills (Collard & McNally, 2009; Dutta et al., 2015; Hilton et al., 2012; Karbou et al., 2010; McNally et al., 2006; Stengel et al., 2009).

Nevertheless, assimilating land surface-sensitive channels remains a global challenge and is still far from operational implementation, particularly over complex terrains. In addition to uncertainties in background LST and LSE, complex terrain introduces pronounced spatial heterogeneity in surface radiation, LST, and boundary-layer thermodynamic structure (Dozier & Outcalt, 1979; Lipton & Ward, 1997; Proy et al., 1989; Robledano et al., 2022; Yan et al., 2016, 2020), which further poses challenges for assimilating surface-sensitive radiance observations in these areas. Garand et al. (2004) highlighted the critical importance of a model's ability to represent fine-scale topography and the associated spatiotemporal variability in LST for effective assimilation of surface-sensitive infrared channels. Dutta et al. (2016) quantitatively demonstrated the high sensitivity of OMB to topographic variability and showed that assimilating surface-sensitive radiance observations becomes more challenging in regions with complex terrain. For instance, for the AIRS 10.7 μm window channel, the standard deviation of OMB across all land regions is 1.37 K, whereas it decreases by approximately 13% to 1.09 K when focusing on flat regions with a terrain standard deviation below 50 m.

The FY-4A Advanced Geosynchronous Radiation Imager (AGRI), China's first next-generation geostationary imager, provides 14-band visible and infrared imagery over East Asia (Yang et al., 2017). The full-disk observational coverage of FY-4A/AGRI spans a wide range of topographic features in China, including plateaus, plains, hills, and basins, with mountainous regions accounting for approximately 67% of the total land area. Such complex terrain causes strong spatial heterogeneity in surface radiation and LST, posing significant challenges for accurately simulating FY-4A/AGRI surface-sensitive infrared BT and effectively assimilating these observations over rugged terrain. While recent work has shown that using satellite-retrieved LST in radiative transfer modeling can help reduce BT discrepancies between model simulation and observation (Li, Huang, et al., 2024; Okabe & Okamoto, 2023), the satellite-retrieved LST is generally restricted to clear-sky condition at satellite's pixels, making it not universal for simultaneously assimilating data from different satellites. For operationally scalable surface-sensitive BT data assimilation, a more fundamental solution lies in improving background LST simulations within NWP models, particularly by reducing physically based, terrain-related systematic biases.

From a model physics perspective, accurately representing terrain-radiation processes (e.g., slope-aspect-dependent solar incidence, terrain shading, and sky-view-controlled scattering/reflection), are essential for reducing biases in surface downward shortwave radiation ($SW_{\downarrow}$) and, consequently, background LST over mountainous regions. Terrain solar radiative effects, such as modulation of solar incidence angles by slope and aspect, terrain shading of direct solar radiation, and the influence of terrain openness on scattered and reflected

10.1029/2025JD045837

radiation, have been well-documented (Chen et al., 2006; Dozier & Frew, 1990; Huang et al., 2022). However, current NWP models often apply the plane-parallel radiation scheme that overlooks the modulation of $SW_{\downarrow}$ by sub-grid topographic variations. This simplification leads to inevitable systematic biases in simulated $SW_{\downarrow}$ over complex topographic regions, failing to capture the non-uniform distribution caused by topographic variability (Arthur et al., 2018; Liou et al., 2013; Manners et al., 2012). Numerous studies have shown that regions with complex topography, such as the Tibetan Plateau (TP), exhibit the most significant errors in surface solar radiation flux simulations in both regional and global weather and climate models (Lee et al., 2011, 2019; Li, Liu, et al., 2021). The deviation between the net surface solar radiation flux calculated without and with TSRE ranges 10–50 W m^{-2} on daily average, and can reach up to 600 W m^{-2} at hourly timescales over TP (Liou et al., 2007). The terrain shading effect can reduce the daily averaged $SW_{\downarrow}$ by 20%–30% (Ineichen, 2008; Tian et al., 2001), and there exists a substantial $SW_{\downarrow}$ anomaly on the order of 200 W m^{-2} between sloped and flat surfaces (Lee et al., 2013). Such modeling biases in $SW_{\downarrow}$ over complex topographic regions can significantly degrade the simulations of LST and land-atmosphere interaction (Chu et al., 2020; Fan et al., 2019; Gu et al., 2012; Hao et al., 2021, 2025), which would in turn exacerbate the satellite surface-sensitive infrared BT simulation biases and cause more observations to fail pre-assimilation quality-control checks, limiting the effectiveness of data assimilation. In this study, we employ the Advanced Weather Research and Forecasting model (WRF-ARW V4.4; Skamarock et al., 2019), incorporating a three-dimensional sub-grid terrain solar radiative effect (3DSTSRE) scheme, to improve the simulations of $SW_{\downarrow}$ and LST. Furthermore, we investigate how reducing terrain-induced biases in $SW_{\downarrow}$ and LST influences the simulation of clear-sky surface-sensitive infrared brightness BT observed by FY-4A/AGRI, which serves as a representative next-generation geostationary infrared imager with high temporal resolution and broad coverage over complex terrain in East Asia. By using FY-4A/AGRI as an independent observational benchmark, this study aims to assess whether improving the physical representation of 3DSTSRE in NWP can effectively mitigate systematic, terrain-dependent biases in modeled $SW_{\downarrow}$ and LST, and consequently in surface-sensitive infrared BT over rugged terrain. The findings are expected to provide practical guidance for improving the use of surface-sensitive infrared radiance observations in regions with complex topography.

In the remaining parts of this paper, after introducing the materials and methods (Section 2), model performance of $SW_{\downarrow}$ and LST will be verified in Section 3. The 3DSTSRE impacts on FY-4A/AGRI clear-sky surface-sensitive infrared BT simulations are given in Section 4. Section 5 summarizes the main findings and offers recommendations for future research.

2. Material and Methods

2.1. Data Sets

The data sets used in this study are summarized below.

1. Radiance observations from AGRI on board the new-generation Chinese geostationary meteorological satellite FY-4A, which was launched on 11 December 2016 and is positioned at 104.7°E (Yang et al., 2017). FY-4A/AGRI provides full-disk imagery every 15 min in 14 spectral bands spanning the visible, near-infrared, and infrared regions, with central wavelengths ranging from 0.47 to 13.5 μm. The spatial resolutions for visible, near-infrared, and infrared bands are 1, 2, and 4 km, respectively. To investigate the physical pathway linking terrain-modulated $SW_{\downarrow}$, LST, and infrared brightness temperature over rugged areas, we focus on three window channels 11–13 with dominant surface sensitivity among the infrared bands. In contrast, upper-level infrared channels, such as water vapor and CO_2 absorption bands, show lower atmospheric transmittance and stronger absorption, resulting in substantially larger atmospheric thermodynamic contributions to the radiances. Including these channels would introduce pronounced atmospheric signals and complicate the attribution of simulated BT differences specifically to background LST improvements induced by the 3DSTSRE scheme.
2. East Asia-Pacific surface longwave/shortwave downward radiation data set from 2016 to 2020 (Letu et al., 2022). The data set has a horizontal resolution of 0.05o and provides 10-min estimates of surface downward longwave and shortwave radiation derived from the next-generation geostationary satellite Himawari-8. It explicitly accounts for the effects of clouds, high aerosol loadings, and topography. The product has high-resolution and all-sky advantages, with significantly higher accuracy at daily and hourly scales compared to other benchmark radiation products.

3. The seamless hourly LST data set with 0.02° resolution over East Asia from 2016 to 2021 (Cheng et al., 2022). The seamless hourly LST product spans 0–60°N and 80–140°E and is generated through a data fusion approach. It combines high-quality hourly clear-sky LST retrieved from Himawari-8/AHI using an improved temperature-emissivity separation algorithm with bias-corrected CLDAS LST through a multiresolution Kalman filter. Independent validation against Heihe Watershed Allied Telemetry Experimental Research in situ observations shows a bias of −0.65 (−0.55) K and a root mean square error (RMSE) of 3.38 (3.03) K under cloudy-sky (all-sky) conditions. In published comparisons, the data set's accuracy is competitive with or better than the original Himawari-8/AHI and other existing all-weather LST products (Dong et al., 2022; Zhou & Cheng, 2020). It outperforms the Meteosat Second Generation SEVIRI all-weather LST product (RMSE 3.8 K; Martins et al., 2019) and geostationary satellites reconstructions using the temporal neighboring-pixel method based on surface energy balance theory (RMSE >5 K at two sites; Lu et al., 2011). Collectively, these results demonstrate a modest yet consistent accuracy advantage, together with an hourly temporal resolution, that is, not available from polar-orbiting all-weather LST products, making this data set particularly well suited for model-based hourly LST evaluation over complex terrain.
4. Integration data set of Tibetan Plateau boundary (Zhang, 2019). The product provides five boundary masks to accurately delineate the plateau's extent from the Pamir Plateau in the west to the Hengduan Mountains in the east, and from the southern edge of the Himalayas to the northern side of the Kunlun-Qilian Mountains. In this study, we use the elevation-based mask TPBoundary-3000 m, which is derived from the ETOPO5 Global Surface Relief to define the TP as areas with elevation ≥3,000 m within the geographic window (20–45°N, 65–105°E).

2.2. Model Description and Experimental Design

WRF-ARW v4.4, a fully compressible and non-hydrostatic model offering multiple parameterization options and flexible resolutions (Skamarock et al., 2019), is employed in this study. To more accurately represent the surface radiation budget over complex terrains, we replace the plane-parallel shortwave treatment in WRF with a recently developed 3DSTSRE scheme (Huang et al., 2022). Following mountain radiation theory (Dozier & Frew, 1990), the scheme partitions the surface downwelling shortwave radiation at a mountainous grid cell into direct ($SW_{\mathrm{dir,ter}\downarrow}$), diffuse ($SW_{\mathrm{dif,ter}\downarrow}$), and terrain-reflected components ($SW_{\mathrm{ref,ter}\downarrow}$). The corresponding computations are given by Equations 1–3:

$$SW_{\mathrm{dir,ter}_\downarrow} = \max\left(\frac{SW_{\mathrm{dir,pla}_\downarrow}}{\cos Z_p} SF_c \mathrm{DIR}_c/\mathrm{SEC}_c, 0\right) \tag{1}$$

$$SW_{\mathrm{dif,ter}_\downarrow} = \begin{cases} SW_{\mathrm{dif,pla}_\downarrow}\left[\frac{SW_{\mathrm{dir,pla}_\downarrow}}{SW_{ac}}\mathrm{SEC}_c + \mathrm{DIF}_c\left(1 - \frac{SW_{\mathrm{dir,pla}_\downarrow}}{SW_{ac}}\right)\right]/\mathrm{SEC}_c, & \mathrm{if DIR}_c > 0 \\ SW_{\mathrm{dif,pla}_\downarrow}\left[\mathrm{DIF}_c\left(1 - \frac{SW_{\mathrm{dir,pla}_\downarrow}}{SW_{ac}}\right)\right]/\mathrm{SEC}_c, & \text{otherwise} \end{cases} \tag{2}$$

$$SW_{\mathrm{ref,ter}_\downarrow} = (SW_{\mathrm{dir,pla}_\downarrow} + SW_{\mathrm{dif,pla}_\downarrow})\gamma \mathrm{REF}_c/\mathrm{SEC}_c \tag{3}$$

where $SW_{\mathrm{dir,pla}_\downarrow}$ and $SW_{\mathrm{dif,pla}_\downarrow}$ are the plane-parallel direct and diffuse components from the WRF shortwave scheme, SW_{ac} denotes the solar constant, and γ is the surface albedo. The grid-scale static topographic correction factors DIR_c, SEC_c, SF_c, DIF_c and REF_c are obtained by aggregating sub-grid terrain characteristics, with the computations given by Equations 4–10:

$$\mathrm{DIR}_c = \cos Z + U_c \sin Z \cos\phi + V_c \sin Z \sin\phi \tag{4}$$

$$\mathrm{SEC}_c = \frac{1}{n}\sum_{i=1}^{i=n} \sec\alpha_i \tag{5}$$

$$SF_c = \frac{1}{n}\sum_{i=1}^{i=n} SF_i \tag{6}$$

10.1029/2025JD045837

$$\mathrm{DIF}_c = \frac{1}{n}\sum_{i=1}^{i=n} \sec \alpha_i \mathrm{SVF}_i \frac{(1+\cos \alpha_i)}{2} \tag{7}$$

$$\mathrm{REF}_c = \frac{1}{n}\sum_{i=1}^{i=n} sec\ \alpha_i \left(\frac{1+\cos \alpha_i}{2} - \mathrm{SVF}_i\right) \tag{8}$$

$$U_c = \frac{1}{n}\sum_{i=1}^{i=n} \tan \alpha_i \cos \beta_i \tag{9}$$

$$V_c = \frac{1}{n}\sum_{i=1}^{i=n} \tan \alpha_i \sin \beta_i \tag{10}$$

where Z and ϕ denote the solar zenith and azimuth angles at the model grid center, and n is the number of sub-grid points within a model grid cell. Each sub-grid point i corresponds to a grid cell from the Shuttle Radar Topography Mission 90 m Digital Elevation Database v4.1 (Jarvis et al., 2008). The sub-grid terrain characteristics α_i, β_i, SF_i and SVF_i represent slope, aspect, shadow factor, and sky view factor, respectively. Specifically, α_i and β_i are derived from the horizontal gradients of elevation (Sharpnack & Akin, 1969; Skidmore, 1989). These two parameters describe the local surface orientation and determine the effective solar incidence angle relative to the terrain surface. SF_i is obtained by comparing the solar elevation angle with maximal topographic elevation angles ε_{ϕ_i} along the solar azimuth angle ϕ_i (Dozier & Frew, 1990). SF_i indicates whether a given sub-grid point is directly illuminated at a given time step. SVF_i quantifies terrain openness and serves as a key parameter controlling the relative contributions of direct, diffuse, and terrain-reflected shortwave radiation received at the surface. Physically, SVF_i is defined as the fraction of visible hemispheric sky at a sub-grid point, and is formulated as the hemispheric integral of unobstructed sky fractions determined by horizon angles H_{ϕ_i}, where $H_{\phi_i} = \pi/2 - \varepsilon_{\phi_i}$, over discrete azimuthal directions (Dozier & Frew, 1990):

$$\mathrm{SVF}_i = \frac{1}{2\pi}\int_0^{2\pi} \left[\begin{array}{c} \cos \alpha \cdot \sin^2 H_{\phi_i} + \sin \alpha \cdot \cos(\phi_i - \beta) \cdot \\ (H_{\phi_i} - \sin H_{\phi_i} \cdot \cos H_{\phi_i}) \end{array} \right] d\phi \tag{11}$$

Lower SVF_i values indicate more obstructed terrain, leading to reduced $SW_\downarrow$ due to enhanced terrain shading and limited sky exposure. Based on this physical interpretation, SVF is subsequently employed as a robust and physically meaningful indicator to categorize terrain complexity in the analysis. The static topographic correction factors are precomputed once, and during runtime, the adjustments are implemented through lookup-table operations, resulting in negligible additional computational cost. Crucially, when 3DSTSRE modifies $SW_\downarrow$ to account for terrain-radiative effects, the corresponding upward shortwave radiation is consistently adjusted using an equivalent surface albedo at the bottom atmospheric level, ensuring grid-scale energy conservation (Hock & Holmgren, 2005; Lee et al., 2015). The 3DSTSRE scheme is computationally efficient and has been shown to improve simulations of surface solar radiation, land-atmosphere interactions, and thus weather and climate dynamics in complex topographic regions (Cai et al., 2023, 2025; Gu et al., 2022, 2024a; Zhang et al., 2022). Further details on the 3DSTSRE formulation and its coupling with WRF can be found in Huang et al. (2022) and Cai et al. (2023). It should be emphasized that the focus of this study is not to refine the algorithm itself, but to evaluate its effectiveness in the context of satellite data assimilation by examining whether 3DSTSRE-induced improvements in $SW_\downarrow$ and LST translate into more accurate clear-sky land surface-sensitive infrared BT simulations over rugged areas.

Two sets of daily rolling forecast experiments, one without and one with 3DSTSRE, hereafter referred to as CTRL and SEN, respectively, are conducted to investigate the impact of 3DSTSRE on simulated $SW_\downarrow$ and LST, as well as their impacts on the FY-4A/AGRI clear-sky surface-sensitive infrared BT simulations. The WRF model domain covers most of East Asia, the northern Indian Ocean, and the northwestern Pacific Ocean (Figure 1). It has a horizontal resolution of 10 km (645 × 475 grid points in the east-west and north-south directions) and 48 vertical levels, with the model top at 10 hPa. As shown in Figure 1, East Asian topography displays a three-step staircase pattern with lower SVF values and more rugged topography over the northwestern, southern, and eastern slopes of TP. The main physical parameterization schemes used are listed in Table 1, including the Noah land surface model (Mitchell et al., 2005), the WRF single-moment 6-class microphysics scheme (Hong & Lim, 2006), the

10.1029/2025JD045837

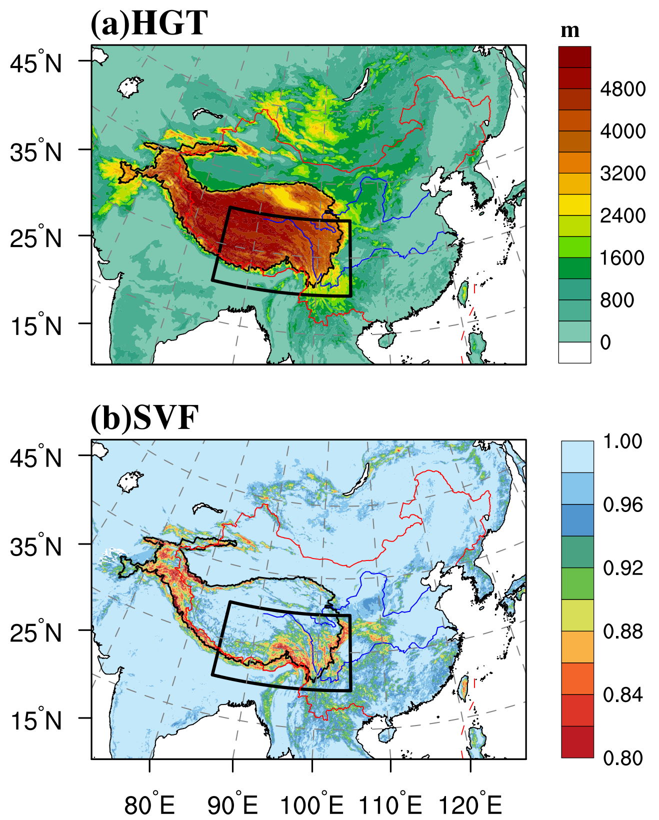

Figure 1. Model domain and spatial distribution of (a) terrain elevation and (b) sky view factor (SVF). The black box highlights the focus area of this study (25°–35°N, 85°–105°E), covering the southeastern Tibetan Plateau (TP) to Sichuan Basin. The red line indicates the national boundary of China. The blue solid lines represent the Yangtze and Yellow Rivers. The black solid line denotes the TP boundary with an elevation of 3,000 m.

Grell-Devenyi ensemble cumulus scheme (Grell & Devenyi, 2002), the Yonsei University planetary boundary layer scheme (Hong et al., 2006), and the CAM shortwave and longwave radiation schemes (Collins et al., 2004). The initial and boundary conditions are generated from the 3-hourly NCEP Global Forecast System real-time forecasts at 0.25° resolution (NCEP, 2015) and the daily global sea surface temperature data set at 0.5° resolution (Thiebaux et al., 2003). The two sets of daily rolling experiments span August 2018 and consist of 36-hr continuous forecasts initialized daily at 12 UTC. The first 12 hr are treated as model spin-up, and the subsequent 24 hr are used for analysis.

The Gridpoint Statistical Interpolation (GSI) system version 3.6 (Hu et al., 2017) is employed to generate the clear-sky BT simulations of three FY-4A/AGRI surface-sensitive infrared channels 11–13, centered at 8.6, 10.8, and 12 μm, respectively. The AGRI instrument has a native spatial resolution of 4 km, and a 20-km data thinning strategy is applied to emulate the assimilation configuration and mitigate the spatial correlation of observation errors. The observation operator used is the Community Radiative Transfer Model (CRTM) version 2.2.3 (Han et al., 2007). Background fields, including three-dimensional atmospheric temperature and humidity and two-dimensional surface variables, are extracted from the CTRL and SEN forecasts. The surface emissivity is obtained from the 0.05°, monthly varying University of Wisconsin-Madison High Spectral Resolution Emissivity atlas for better surface-sensitive radiance simulations (Seemann et al., 2007). The cloud mask products are obtained from the official FY-4A/AGRI data set (Wang et al., 2019).

2.3. Analysis Methodology

Both observed and simulated $SW_{\downarrow}$ and LST fields are bilinearly interpolated (Shepard, 1968) onto the 20-km thinned AGRI grid points to ensure spatial consistency in the comparison. This approach follows the standard practice in the GSI system for mapping model background fields to observation locations, and is well-suited for downscaling higher-resolution fields to the coarser target grid required by the data thinning strategy. We acknowledge that interpolation methods, including bilinear interpolation, have inherent limitations in resolving terrain-induced spatial variability of $SW_{\downarrow}$ and LST. However, by applying the same interpolation method to both observed and simulated fields, systematic interpolation-related biases are minimized, allowing a fair comparison focused on the relative improvements brought by the 3DSTSRE scheme. Model performance is assessed using pattern correlation (PC), mean bias (BIAS), and RMSE. Specifically, PC ranges from −1 to 1, with larger magnitudes indicating greater similarity between observations and simulations. Smaller absolute BIAS and RMSE indicate that the simulated values are closer to the observed magnitude values. Further details of the statistical metrics are provided in Wu et al. (2019).

Table 1
WRF Physical Parameterization Schemes

Physics	Scheme
Land surface model	Noah (Mitchell et al., 2005)
Microphysics	WRF single-moment 6-class scheme (Hong & Lim, 2006)
Cumulus parameterization	Grell-Devenyi ensemble scheme (Grell & Devenyi, 2002)
Planetary boundary layer	Yonsei University scheme (Hong et al., 2006)
Shortwave radiation	CAM scheme (Collins et al., 2004)
Longwave radiation	CAM scheme (Collins et al., 2004)

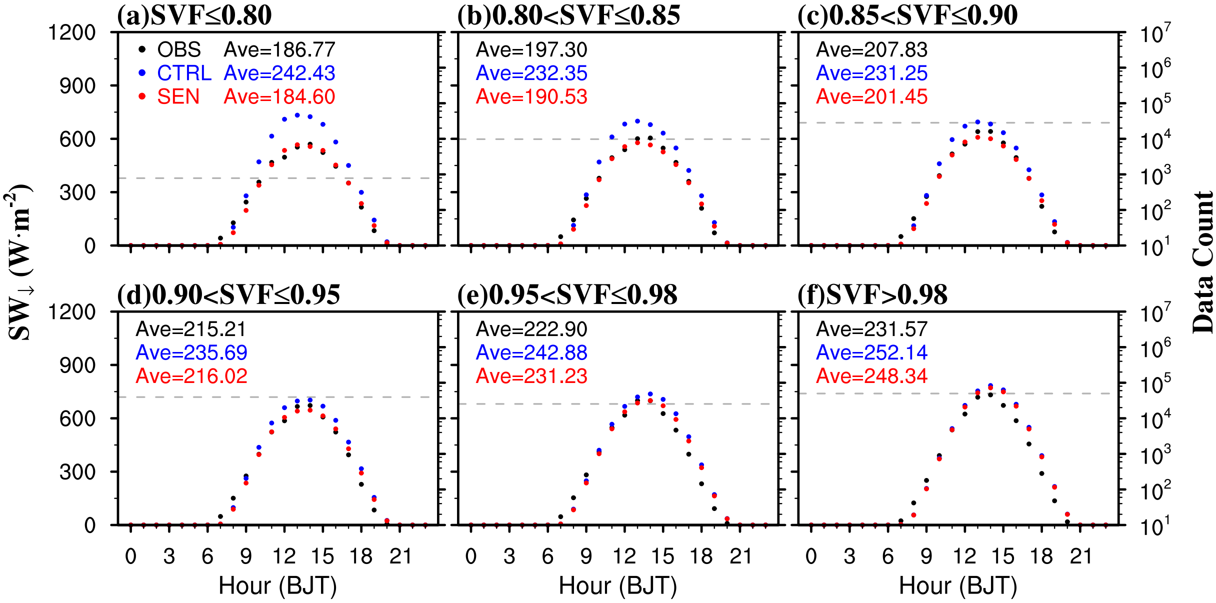

Figure 2. Diurnal variations of surface downward solar radiation ($SW_{\downarrow}$, unit: Wm^{-2}) within different SVF categories, averaged over the study area (25°–35°N, 85°–105° E) for all days in August 2018: (a) Himawari-8 radiation products (black dots), simulations from (b) CTRL (blue dots) and (c) SEN (red dots) experiments. The dashed lines represent the data count, and the text Ave denotes the daily mean $SW_{\downarrow}$. The text BJT below the horizontal axis represents Beijing Time.

To investigate the impacts of 3DSTSRE on simulated $SW_{\downarrow}$, LST, and BT over complex terrain in more detail, we focus on the southeastern slope of TP extending into the Sichuan Basin (25°–35°N, 85°–105°E), a region of pronounced topographic variability (Figure 1b). Following Li, Huang, et al. (2024), we employ a flat-region OMB subtraction to reduce the systematic BT bias arising from uncertainties in land surface parameters (e.g., LST and LSE) and in the radiative transfer operator. This step helps isolate the signal of terrain-induced variability in the BT simulations. Concretely, for each grid point in the study region, we compute the mean clear-sky OMB over flat areas (SVF >0.99) within a 1° × 1° latitude-longitude box and define this mean as the systematic error (μ). The value of μ is calculated separately for both experiments at each analysis hour to enhance the robustness of diurnal variation in bias correction. Finally, by subtracting μ, we derive the residual bias that effectively isolates the clear-sky OMB attributed to terrain heterogeneity (OMB_{ter}). It should be noted that the clear-sky samples used for BT evaluation are identified based on the official FY-4A/AGRI cloud mask product (Wang et al., 2019). For each 20-km thinned AGRI grid point, only those pixels classified as clear-sky by the satellite observations are retained, and the same set of clear-sky samples is applied consistently to both the CTRL and SEN experiments. This observation-based sampling strategy avoids inconsistencies arising from model-dependent cloud simulations, ensuring a fair comparison of model performance under actual clear-sky conditions, so that the evaluated BT differences primarily reflect 3DSTSRE-induced changes in surface shortwave radiation and background LST.

3. Model Evaluation

3.1. Surface Downward Solar Radiation

Figures 2 and 3 present the diurnal variations and statistical characteristics of $SW_{\downarrow}$ across different SVF categories, averaged over the study region for August 2018, using the Himawari-8 satellite product and results from the two experiments. In general, when a surface point is partially shaded by surrounding terrain, more complex topography (i.e., smaller SVF) leads to less downward shortwave flux reaching the surface, whereas flatter terrain (i.e., SVF approaching 1) leads to higher $SW_{\downarrow}$. The Himawari-8 product clearly captures the influence of terrain shading on $SW_{\downarrow}$ distribution. Quantitatively, as SVF decreases from greater than 0.98 to less than 0.80, the daily mean observed $SW_{\downarrow}$ decreases from 231.57 to 186.77 Wm^{-2} (Figures 2a and 2f). CTRL experiment reproduces the diurnal cycle and peak time (~14:00 Beijing Time, hereafter BJT) of $SW_{\downarrow}$ but evidently overestimates its magnitude, with BIAS increasing rapidly as terrain complexity increases (Figures 2 and 3). For instance, as SVF decreases from greater than 0.98 to less than 0.80, BIAS increases by more than a factor of two, from 20.57 to

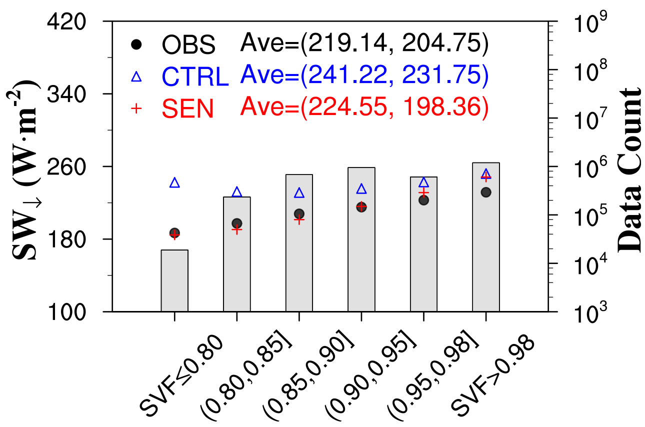

Figure 3. $SW_{\downarrow}$ from Himawari-8 radiation products (black dots), CTRL (blue triangles) and SEN (red crosses) simulations within different SVF categories, averaged over the study area (25°–35°N, 85°–105°E) for all days in August 2018. The gray bars represent data count within each SVF bin, and the text Ave represents the data count-weighted average for all cases (first value in parentheses) and for cases where SVF is less than 0.9 (second value in parentheses).

55.66 Wm^{-2} (Figures 2a and 2f). With 3DSTSRE incorporated, SEN experiment effectively mitigates the terrain-dependent $SW_{\downarrow}$ BIAS (Figure 3). The most pronounced reductions in the BIAS of simulated $SW_{\downarrow}$ occur under low to intermediate SVF conditions, corresponding to complex terrain where terrain-induced shading and sky obstruction are significant. When SVF exceeds 0.95, terrain-radiative effects weaken, and $SW_{\downarrow}$ becomes increasingly dominated by atmospheric conditions and surface albedo rather than topographic modulation. Under such near-flat conditions, the impact of 3DSTSRE is inherently limited, and the $SW_{\downarrow}$ simulation BIAS is slightly reduced or persists. This behavior indicates that the proposed scheme is primarily designed to enhance $SW_{\downarrow}$ simulations over complex terrain, and maintains physically consistent performance over relatively flat regions where terrain-radiative effects are intrinsically weak. Compared with CTRL, domain-mean BIAS in SEN decreases by 76.86% from 22.08 to 5.11 Wm^{-2} (Figure 3), and in regions with SVF less than 0.80, it decreases more substantially from 55.66 to −2.17 Wm^{-2} (Figure 2a).

Figure 4 illustrates the spatial distribution of mean $SW_{\downarrow}$ in August 2018 for regions with SVF less than 0.9 from the Himawari-8 radiation product and two experiments, as well as with their differences. These regions are primarily located in the northwest-southeast-oriented Hengduan Mountains and the east-west-oriented Qinling-Daba Mountains. Both simulations capture the overall pattern of $SW_{\downarrow}$ in these regions, with PCs exceeding 0.98 (Figures 4a–4c). However, CTRL substantially overestimates $SW_{\downarrow}$, especially along the periphery of TP, where topographic variability is pronounced. This results in a regional-mean overestimation of 27.00 Wm^{-2} (Figure 4d). As shown in Figure 4f, the inclusion of 3DSTSRE effectively reduces the positive $SW_{\downarrow}$ BIAS caused by the plane-parallel radiation scheme, bringing the regional-mean $SW_{\downarrow}$ in SEN (198.36 Wm^{-2}) much closer to the observed value (204.75 Wm^{-2}).

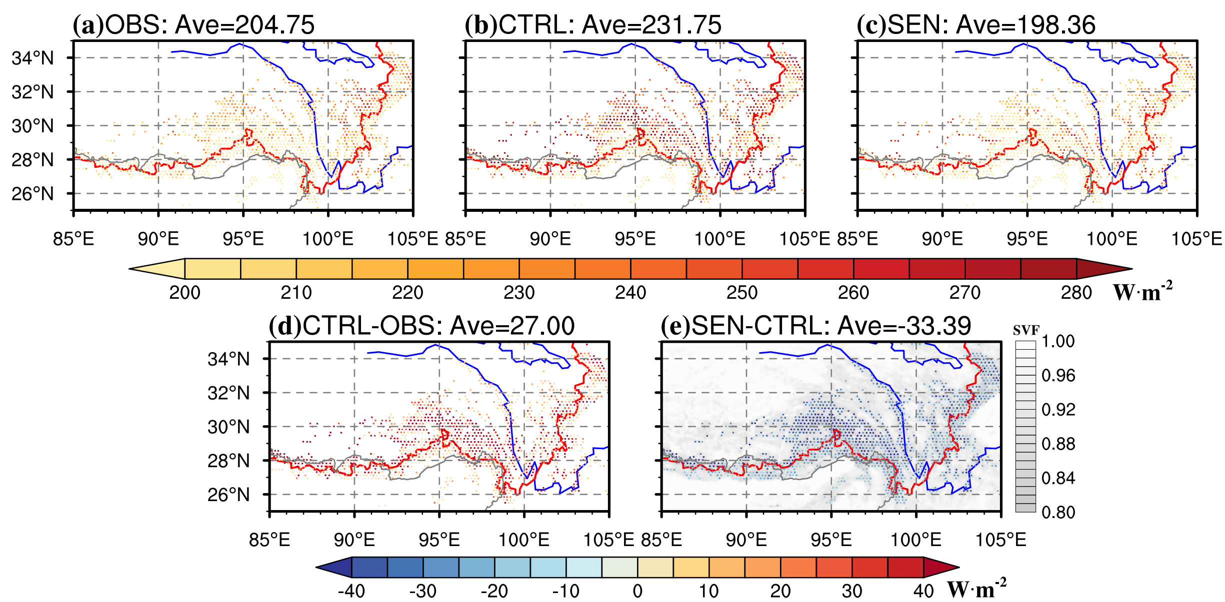

Figure 4. Spatial distributions of mean $SW_{\downarrow}$ in August 2018 over the regions with SVF less than 0.9: (a) Himawari-8 radiation products, simulations from (b) CTRL and (c) SEN experiments, the differences (d) between CTRL and observations, and (e) between SEN and CTRL, with the domain-mean depicted by the text Ave. The shadings in (e) denote the spatial distribution of SVF. The gray line indicates the national boundary of China. The blue solid lines represent the Yangtze and Yellow Rivers. The red solid line denotes the TP boundary with an elevation of 3,000 m.

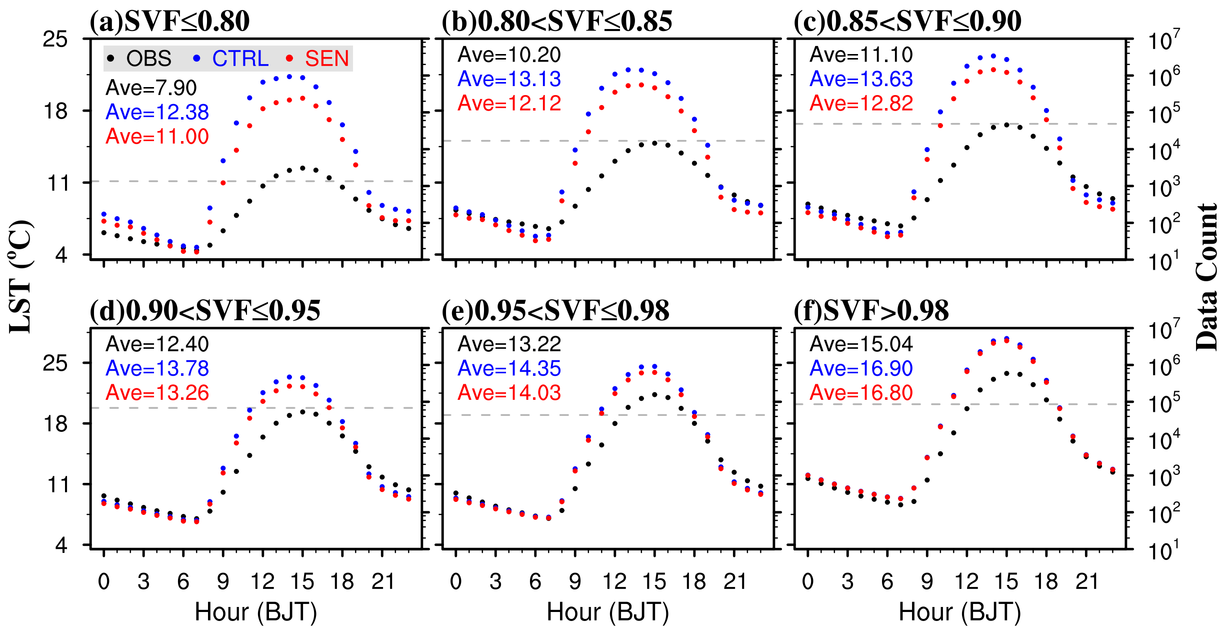

Figure 5. Same as Figure 2, but for land surface temperature (LST, unit: °C). LST OBS is from the Himawari-CLDAS fused product.

3.2. Land Surface Temperature

Because the accuracy of surface-sensitive infrared BT simulations strongly depends on the quality of background LST, we next evaluate the impact of the 3DSTSRE scheme on LST simulation performance. Figure 5 shows the diurnal variations of LST within different SVF categories, based on the Himawari-CLDAS fused product and the two experiments, averaged over all days during August 2018. Consistent with the diurnal pattern of $SW_{\downarrow}$, the fused LST peaks around 14:00 BJT and drops to its minimum during nighttime (19:00-07:00 BJT of the following day). The product also captures the terrain-shading effects on $SW_{\downarrow}$ and the resulting influence on LST, showing a decrease in regional-mean LST with increasing topographic complexity. Compared with observations, the CTRL experiment captures the diurnal phase and shows small BIAS during nighttime, but exhibits notable BIAS during daytime (08:00–18:00 BJT) across all SVF categories, especially over complex terrain with SVF less than 0.90. Benefiting from the improved representation of terrain-dependent $SW_{\downarrow}$ through 3DSTSRE scheme, SEN experiment effectively alleviates the daytime LST overestimation over complex terrain. For example, in regions with SVF less than 0.80, the mean positive BIAS is reduced by 30.80%, from 4.48°C to 3.10°C (Figure 5). However, under the daily rolling forecast framework, soil temperature anomalies remain confined to the near surface and dissipate rapidly through land-atmosphere interactions, leading to minimal nighttime LST differences between the two experiments.

Figure 6 compares the simulated LST from the two experiments across different SVF categories under all-sky and clear-sky conditions. The domain-mean LST BIAS is smaller under clear-sky conditions than under all-sky conditions (all-sky: CTRL 1.89°C, SEN 1.44°C; clear-sky: CTRL 0.71°C, SEN 0.26°C). In complex terrain with SVF less than 0.90, CTRL experiment shows significantly larger LST BIAS under both sky conditions, corresponding to the pronounced positive terrain-dependent $SW_{\downarrow}$ BIAS. Compared with CTRL, SEN experiment reduces the BIAS in complex terrain (SVF ≤ 0.90) by 32.13% (from 2.77°C to 1.88°C) under all-sky conditions (Figure 6a), and by 61.18% (from 1.70°C to 0.66°C) under clear-sky conditions (Figure 6b). As $SW_{\downarrow}$ is a key component of the surface energy budget, incorporating 3DSTSRE improves the $SW_{\downarrow}$ simulation over complex terrain and consequently enhances the modeled daytime LST, with the largest improvements under clear-sky conditions (Figure 6b). Nevertheless, residual LST BIAS over complex terrain, especially under all-sky conditions (Figure 6a), persists, indicating that further improvements are required in other energy-balance components (e.g., longwave radiation and turbulent fluxes). Since this study focuses on enhancing the clear-sky surface-sensitive infrared BT simulation over complex terrain, the current scheme's effectiveness in reducing terrain-dependent $SW_{\downarrow}$ and clear-sky LST BIAS is encouraging and contributes directly to this objective.

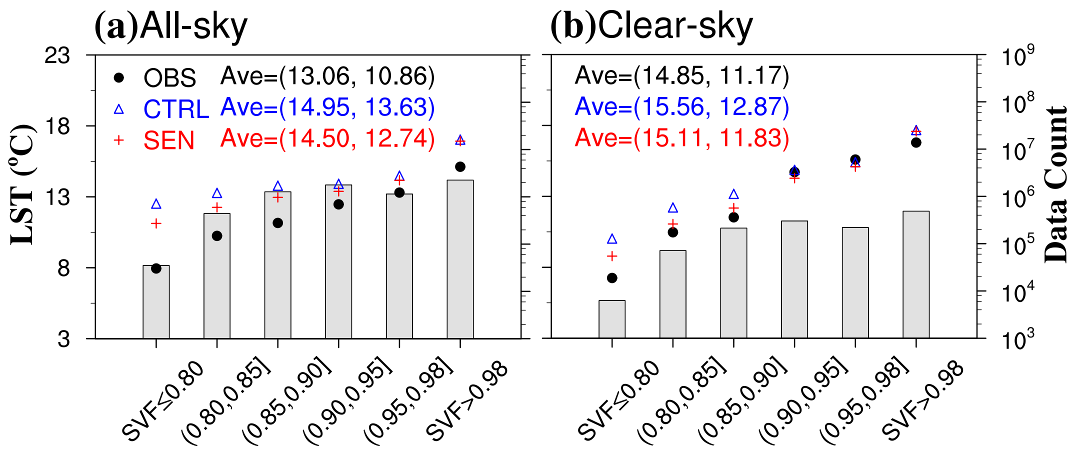

Figure 6. Same as Figure 3, but for (a) all-sky and (b) clear-sky land surface temperature, respectively.

Figure 7 further shows the spatial distribution of daytime clear-sky LST from the Himawari-CLDAS fused product and the two experiments over complex terrain (SVF ≤ 0.90). The CTRL experiment clearly overestimates LST in these regions, with a regional-mean positive bias of 3.01°C (Figures 7a, 7b, and 7d). Incorporating 3DSTSRE effectively reduces the daytime positive LST BIAS in SEN, lowering the regional-mean value by 36.54% from 3.01°C to 1.91°C (Figures 7d and 7e). This improvement is consistent with the correction of the positive terrain-dependent $SW_{\downarrow}$ BIAS (Figure 4), with the strongest effects along the periphery of the Tibetan Plateau, where topographic variability is most pronounced.

4. LST Impacts on FY-4A/AGRI Clear-Sky Surface-Sensitive Infrared BT Simulations

In this section, we explore whether the enhanced clear-sky LST fields brought by the updated 3DSTSRE scheme in WRF translate into more accurate clear-sky BT simulations for the FY-4A/AGRI surface-sensitive channels. Figure 8 compares clear-sky BT OMB_{ter} across different SVF categories for all times of day, daytime, and nighttime, based on both experiments during August 2018. Figure 9 presents the diurnal variation and statistical evaluation of OMB_{ter} over complex terrain with SVF ≤ 0.90. As shown in Figure 8, CTRL experiment exhibits notable negative terrain-dependent OMB_{ter} across all three FY-4A/AGRI surface-sensitive channels regardless of

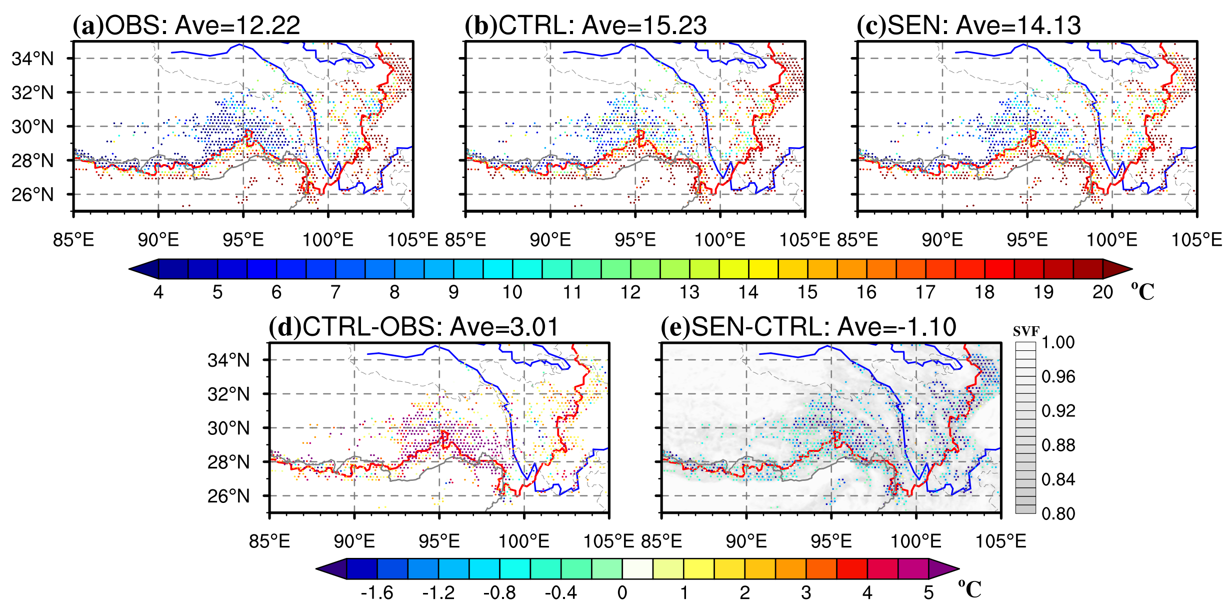

Figure 7. Same as Figure 4, but for clear-sky land surface temperature during daytime (08:00–18:00 BJT).

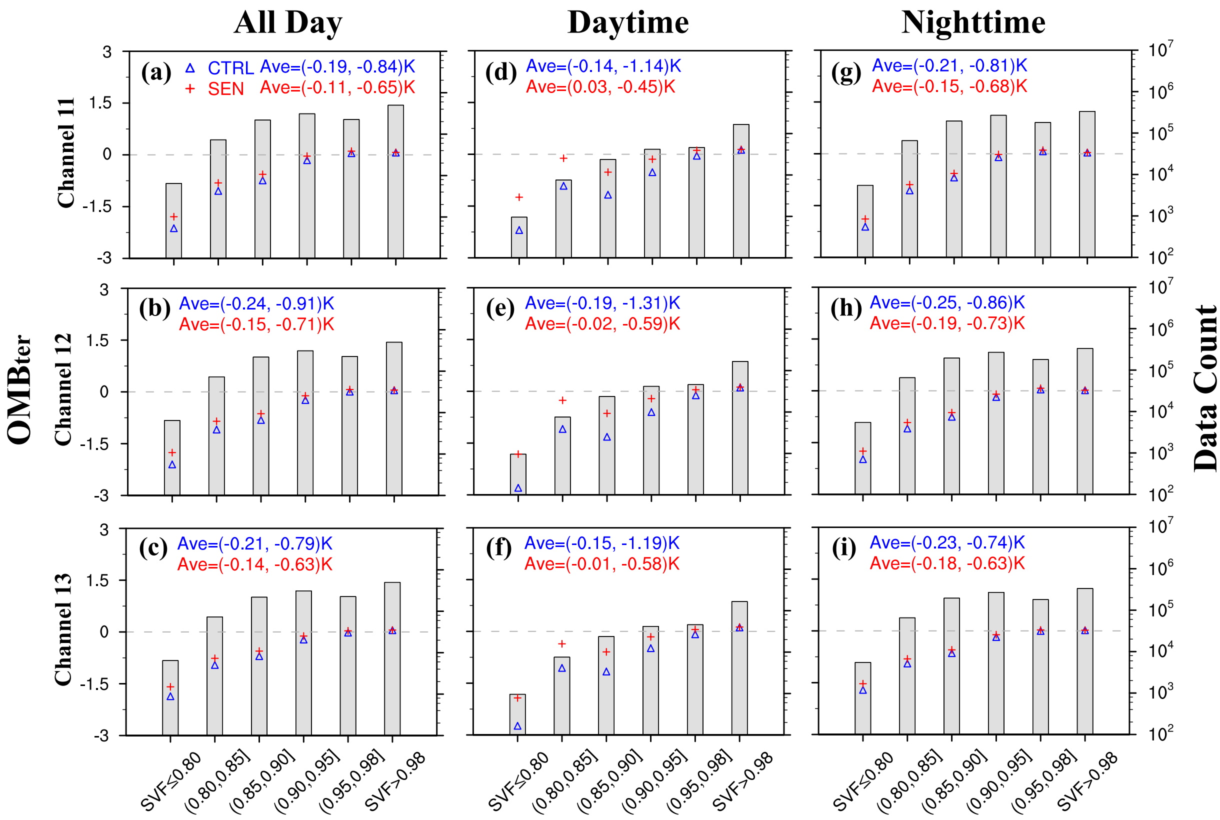

Figure 8. Left column: Clear-sky brightness temperature (BT) observation-minus-background bias attributed to terrain heterogeneity (OMB_{ter}, unit: (K) of channels (a) 11, (b) 12, and (c) 13 within different SVF categories, averaged over the study area (25°–35°N, 85°–105°E) for all times of day in August 2018. The mid and right columns are the same as the left column but for daytime and nighttime statistics, respectively. The formats of Ave and Gy bars are consistent with those in Figure 3.

the time of day (all day, daytime, or nighttime). The largest deviations occur in regions with SVF ≤ 0.90, which are topographically complex and characterized by significant slope/aspect contrasts, frequent terrain shading, and partial sky obstruction. These regions include mountainous areas with pronounced slope/aspect variations, deep valleys, plateaus, and rugged hills, primarily located in the northwest-southeast-oriented Hengduan Mountains and the periphery of TP (Figures 4 and 7). This pattern arises due to the CTRL configuration of plane-parallel shortwave radiation scheme, which causes systematic, terrain-dependent overestimation of $SW_{\downarrow}$, LST, and BT, and consequently leads to negative OMB_{ter} statistics for the window channels. Relative to CTRL, SEN experiment improves the BT simulations for all three channels, reducing the mean OMB_{ter} over SVF ≤ 0.90 regions by 22.62%, 21.98%, and 20.25%, from −0.84, −0.91, and −0.79 K to −0.65, −0.71, and −0.63 K, respectively (Figures 8a–8c). Consistent with the correction of daytime positive terrain-dependent $SW_{\downarrow}$ and clear-sky LST BIAS by 3DSTSRE, the clear-sky BT improvements also exhibit a distinct diurnal contrast, with more pronounced reductions during daytime than nighttime (Figures 8d–8i, and 9). Specifically, during daytime over complex terrain, OMB_{ter} decreases by 60.53%, 54.96%, and 51.26%, from −1.14, −1.31, and −1.19 K in CTRL to −0.45, −0.59, and −0.58 K in SEN, respectively (Figures 8d–8f, and 9d). The RMSE values are likewise substantially reduced from 1.64, 1.85, and 1.72 K to 1.16, 1.35, and 1.32 K (Figure 9f). During nighttime, both the mean OMB_{ter} and RMSE show only modest improvements (Figures 8g–8i, 9e, and 9g). The distinct diurnal contrast in clear-sky BT improvements reflects the physical processes represented by the 3DSTSRE scheme. As the scheme focuses on improving the model representation of terrain-modulated shortwave radiative effects (Dozier & Frew, 1990; Huang et al., 2022), its impacts on $SW_{\downarrow}$, LST, and BT simulations are confined to daytime conditions when solar radiation is present. During the night, solar radiation vanishes and the surface energy balance is dominated by longwave radiative exchange and turbulent heat fluxes. In the current model configuration, sub-grid terrain longwave radiative effects (Gu et al., 2024b), e.g., terrain obstruction of atmospheric longwave radiation and longwave emission from surrounding slopes, are not explicitly represented. Consequently, nighttime LST evolution and the associated BT simulations are weakly affected by the inclusion of

10.1029/2025JD045837

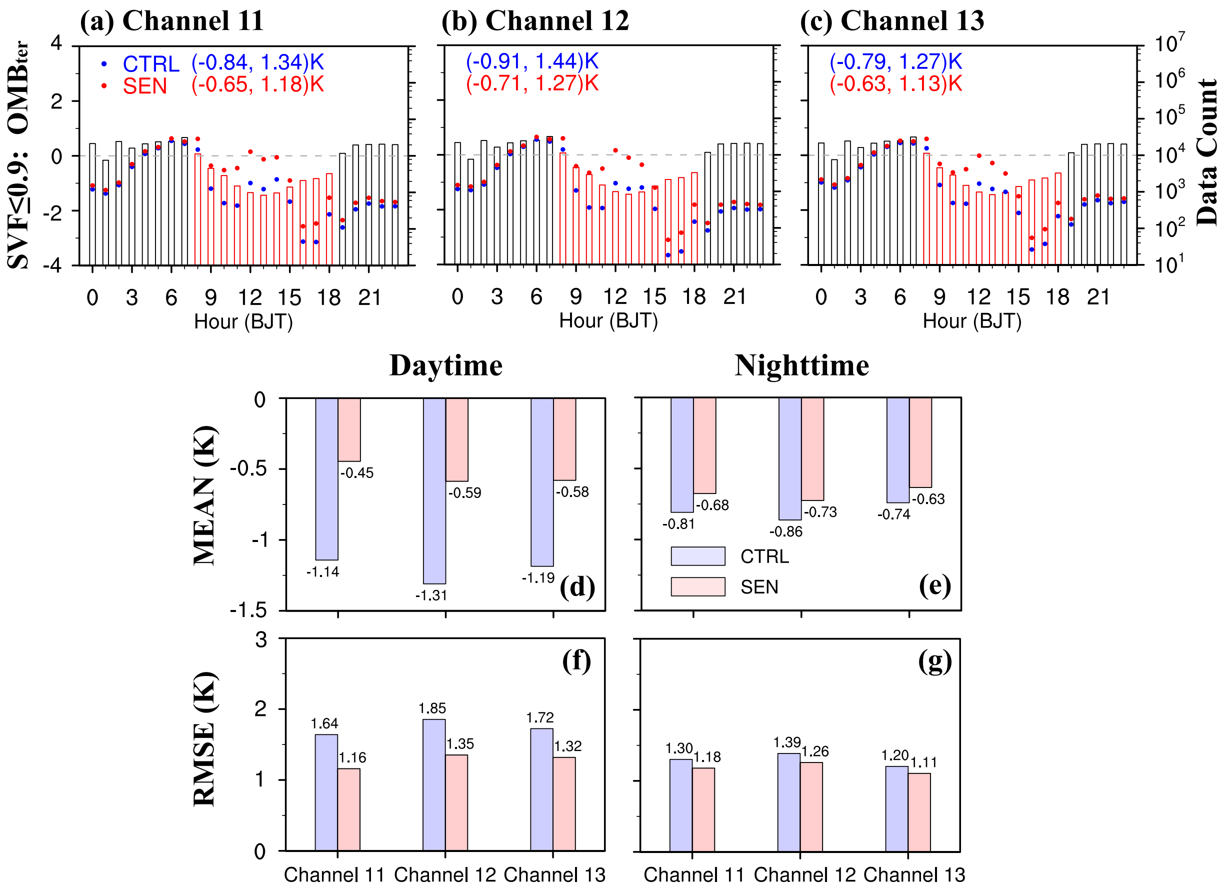

Figure 9. Diurnal variations of clear-sky OMB_{ter} (unit: (K) of channels (a) 11, (b) 12, and (c) 13 averaged over the study area (25°–35°N, 85°–105°E) with SVF less than 0.9 for all days in August 2018, with the daily mean (first value) and root mean square error (RMSE) (second value) given in parentheses. In (a–c), the red and black bars indicate the data count during daytime (08:00–18:00 BJT) and nighttime (19:00 BJT-07:00 BJT of the following day), respectively. (d, e) give the mean of clear-sky OMB_{ter} for three channels during daytime and nighttime, respectively. Panels (f, g) are same as (d, e), but for RMSE.

3DSTSRE, leading to much smaller differences between CTRL and SEN. The residual impacts are mainly limited to the early evening, reflecting the persistence and gradual dissipation of daytime thermal anomalies through land-atmosphere interactions under the daily rolling forecast framework. The diurnal variation in the number of clear-sky samples over regions with SVF $\leq$ 0.90 primarily reflects the characteristic mountain-valley circulation pattern: during daytime, especially in the afternoon, persistent solar heating of mountain slopes triggers thermally driven upslope winds and convective cloud development, substantially reducing the number of clear-sky pixels; whereas at night, surface radiative cooling generates downslope flows and a more stable boundary layer that suppresses convection and cloud formation, yielding more available clear-sky samples.

Next, we analyze the spatial distributions of observed clear-sky BT and simulated OMB_{ter} from both experiments for the three surface-sensitive FY-4A/AGRI channels during daytime in August 2018, focusing on complex terrain with SVF less than 0.9 (Figure 10). The observed daytime clear-sky BT exhibits higher values in low-elevation areas and lower values over the high-altitude interior of TP (Figures 10a1–a3). Both experiments reasonably capture the overall spatial pattern of clear-sky BT with PCs exceeding 0.96. However, CTRL experiment markedly overestimates BT, resulting in a negatively skewed OMB_{ter} distribution (Figures 10b1–b3). Incorporating 3DSTSRE effectively mitigates this BT overestimation over topographically complex regions (Figures 10c1–10c3). These results highlight the importance of integrating 3DSTSRE into the radiative-transfer parameterization to more accurately represent terrain-dependent $SW_{\downarrow}$ and clear-sky LST, thereby improving BT simulations over heterogeneous terrain.

10.1029/2025JD045837

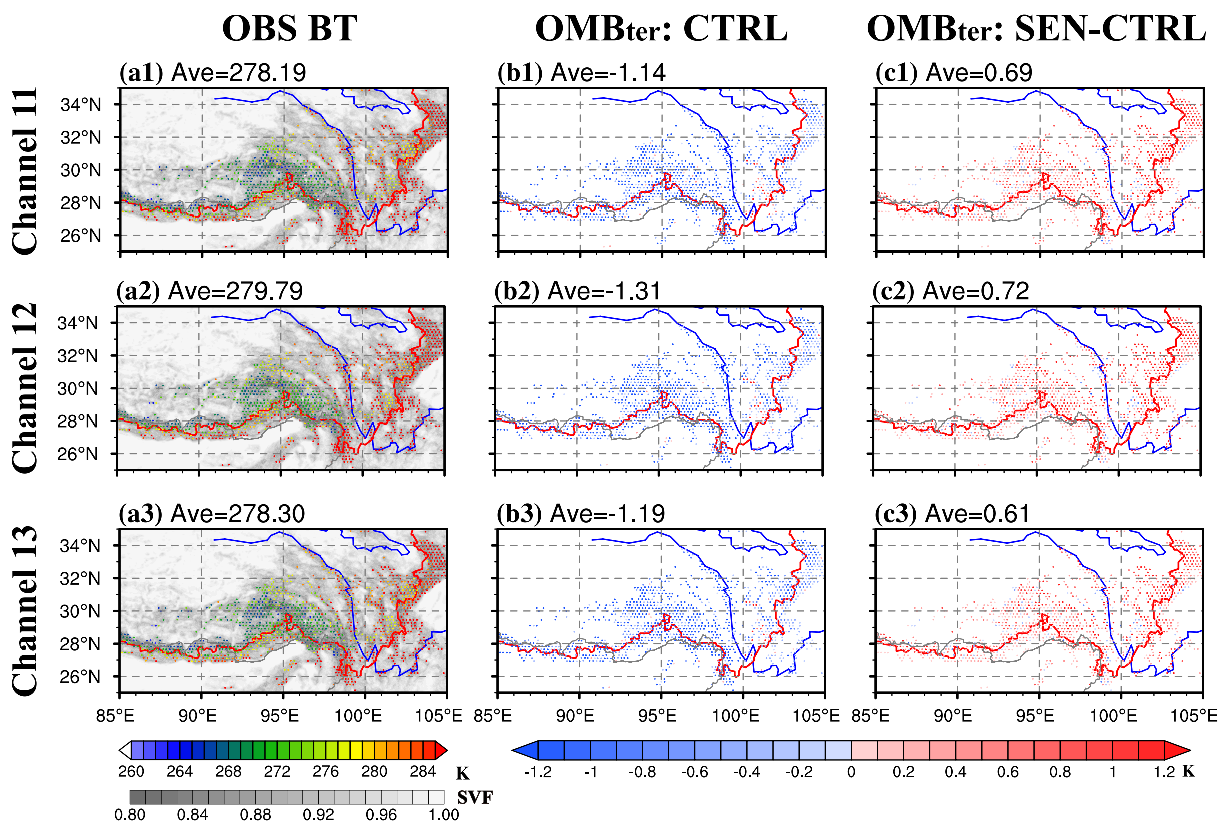

Figure 10. Spatial distributions of observed clear-sky BT (first column), simulated OMB_{ter} in CTRL experiment (middle column) and its difference with SEN experiment (third column) over regions with SVF less than 0.9 during daytime in August 2018. Results are shown for channels 11 (first row), 12 (second row), and 13 (third row). The text Ave denotes the domain-mean value. The formats of gray, blue and red lines are the same as those in Figure 4.

5. Summary, Discussion and Future Recommendations

Accurate simulation of satellite surface-sensitive infrared BT over complex terrain critically depends on the representation of background LST and its controlling radiative processes. These processes are strongly influenced by topographic effects on $SW_{\downarrow}$, which remain inadequately represented in most current NWP models. This study evaluates the impact of incorporating a 3DSTSRE scheme into WRF on the simulations of $SW_{\downarrow}$ and LST, and consequently on clear-sky BT simulations of FY-4A/AGRI surface-sensitive channels over rugged terrain.

For the study domain spanning the southeastern slope of TP to Sichuan Basin (25°–35°N, 85°–105°E), CTRL experiment (without 3DSTSRE) produces substantial terrain-dependent overestimations in both $SW_{\downarrow}$ and LST, particularly in regions with high topographic complexity (SVF $\leq$ 0.90). The incorporation of the 3DSTSRE scheme in the SEN experiment effectively mitigates these biases. Specifically, the domain-mean $SW_{\downarrow}$ BIAS is reduced by 76.86% from 22.08 to 5.11 Wm^{-2}, and over rugged terrain with SVF less than 0.80, it decreases even more markedly, from 55.66 to −2.17 Wm^{-2}, bringing the simulations much closer to satellite estimates. This improvement in simulated $SW_{\downarrow}$ directly leads to a notable reduction in the daytime positive terrain-dependent LST BIAS. Over rugged terrain with SVF $\leq$ 0.90, the all-sky LST BIAS is reduced by 32.13% (from 2.77°C to 1.88°C), while the clear-sky LST BIAS decreases by 61.18% (from 1.70°C to 0.66°C).

The improved clear-sky LST fields resulting from the 3DSTSRE scheme further contribute to reducing terrain-induced biases in the simulated clear-sky BT for FY-4A/AGRI channels 11–13. Notable improvements are observed during daytime hours, as $SW_{\downarrow}$ and LST anomalies generated under the daily rolling forecast framework dissipate rapidly after sunset through land-atmosphere interactions. Over rugged terrain with SVF $\leq$ 0.90, the daytime clear-sky BT OMB_{ter} for channels 11, 12, and 13 decreases from −1.14, −1.31, and −1.19 K in CTRL to −0.45, −0.59, and −0.58 K in SEN, corresponding to reductions of 60.53%, 54.96%, and 51.26%, respectively.

10.1029/2025JD045837

It is important to interpret the sign difference of OMB_{ter} relative to that reported by Li, Huang, et al. (2024). In our CTRL configuration, the plane-parallel shortwave radiation treatment leads to $SW_{\downarrow}$ overestimation, producing a daytime positive LST BIAS over complex terrain. Because the BT simulations are driven by the modeled LST, this warm background translates into negative OMB_{ter} values in the window channels. By contrast, Li, Huang, et al. (2024) used FY-4A/AGRI-retrieved LST to drive the CRTM, which avoids the model LST systematic bias.

We employ the Himawari-8 $SW_{\downarrow}$ retrieval product of Letu et al. (2022) as an observational benchmark because it explicitly applies a topographically corrected shortwave radiation model (SWTRM; Wang et al., 2018), which effectively captures the spatial variability of $SW_{\downarrow}$ over mountainous regions, including contrasts between sunny and shaded slopes. Although both SWTRM and 3DSTSRE incorporate key terrain-radiation processes highlighted by mountain radiation theory (Dozier & Frew, 1990), e.g., slope-aspect-dependent solar incidence, terrain shading, sky-view-controlled diffuse radiation, and terrain-reflected radiation, their design objectives and implementation strategies differ fundamentally. SWTRM is an offline satellite retrieval algorithm that requires precomputing radiation values under various atmospheric and surface conditions using radiative transfer models (e.g., MODTRAN) to build a lookup table (LUT). During real-time retrieval, satellite observation parameters are matched against the LUT to derive surface radiation. The algorithm must handle topographic obstruction from both solar and sensor viewing geometries, and in cases of complete sensor obstruction, it approximates radiation fluxes using nearby non-shaded pixels as a gap-filling strategy (Tovar et al., 1995). By contrast, 3DSTSRE is designed as an online NWP parameterization aimed at improving grid-mean shortwave radiation simulations over mountainous regions. It represents the sub-grid terrain-radiative effects through aggregated topographic correction factors that can be directly applied to the model's prognostic upwelling and downwelling shortwave components. The scheme is formulated to maintain physical consistency with the grid-scale surface energy balance, ensuring numerical stability and operational feasibility. Therefore, Himawari-8 serves as an independent, high-quality terrain-corrected reference for evaluation, while SWTRM itself is not directly applicable within NWP models due to its retrieval-oriented design and reliance on observation geometry and cross-pixel approximations.

Overall, 3DSTSRE scheme effectively improves $SW_{\downarrow}$ simulations over rugged terrain, thereby alleviating clear-sky LST overestimation and the associated negative OMB_{ter} BIAS in clear-sky BT for FY-4A/AGRI surface-sensitive channels. Over relatively flat and open terrain with SVF approaching 1, terrain-radiative effects are intrinsically weak. As expected, the impacts of 3DSTSRE on $SW_{\downarrow}$, LST, and subsequent BT simulations are marginal, with model performance maintaining consistent with the original plane-parallel shortwave radiation treatment. These results demonstrate a clear terrain-regime dependence of 3DSTSRE impacts, with the largest benefits occurring in regions characterized by pronounced sub-grid topographic heterogeneity, such as strong slope and aspect contrasts, frequent terrain shading, and sky obstruction, typically associated with low to medium SVF. It is important to address whether the improved agreement of SEN with Himawari-8 $SW_{\downarrow}$ product reflects physical improvement or error cancellation between model and satellite retrieval biases, given that any single satellite product contains retrieval uncertainties over complex terrain. First, the modeled $SW_{\downarrow}$, LST, and BT are evaluated against three independent reference data sets, and the improvement chain is found across all SVF categories, with the most pronounced improvement over complex terrain where 3DSTSRE physical corrections are strongest. Such a physically coherent, multi-variable, terrain-dependent improvement pattern would not be expected under the error cancellation hypothesis. Moreover, the effectiveness of 3DSTSRE scheme in correcting terrain-induced $SW_{\downarrow}$ biases has been validated by prior studies (Gu et al., 2022; Zhang et al., 2022, 2024) against multiple independent benchmarks beyond Himawari-8, including the Global Land Surface Satellite product (Liang et al., 2021), the CLARA product (Karlsson et al., 2017), and the in situ automatic weather station data within the Heihe Integrated Observatory Network (Liu et al., 2016a, 2016b, 2018). The prior studies, employing different models and focusing on different regions, provide corroborative evidence that the effectiveness of the 3DSTSRE scheme is physically based rather than coincidental matching of a particular satellite product. These findings further imply a broader applicability of the proposed framework for improving clear-sky surface-sensitive infrared BT simulations in regions with non-negligible topographic heterogeneity beyond the southeastern Tibetan Plateau-Sichuan Basin study area.

Despite these improvements, several limitations remain, suggesting directions for future work. First, non-negligible OMB_{ter} persists over rugged terrain. This may be partly attributed to the omission of terrain-induced longwave radiation effects in current models, which can influence the surface longwave radiation

10.1029/2025JD045837

balance and LST simulations. Recent studies suggest that accounting for terrain-induced atmospheric downwelling longwave radiation shielding and longwave emission from adjacent slopes could further refine simulations of the surface energy balance and near-surface thermodynamic profiles over mountainous regions (Gu, Huang, Li, Yang, Wu, 2024; Gu et al., 2024b). Second, although the 3DSTSRE scheme explains much of the clear-sky LST BIAS, discrepancies in other land-atmosphere interaction processes also contribute to residual errors. Future efforts should focus on a more comprehensive attribution of LST BIAS by refining the parameterizations of surface roughness length (Li, Liu, et al., 2021; Zhou et al., 2022), vegetation cover, and surface emissivity (Li et al., 2019; Ma et al., 2019). Enhancing the LST simulation accuracy through improved representation of key land-atmosphere interaction processes is expected to further enhance surface-sensitive infrared BT simulations (Trigo et al., 2015; Zheng et al., 2012). Third, we note that WRF simulations can be sensitive to the choice of initial and lateral boundary conditions (IC/LBCs; Gallus & Bresch, 2006; Kumar et al., 2017; Toth & Kalnay, 1993). In this study, CTRL and SEN employ identical IC/LBCs, and thus the reported differences primarily reflect the impact of the 3DSTSRE scheme rather than uncertainties related to IC/LBC. Nevertheless, the absolute magnitudes of the simulated fields may vary under alternative IC/LBC data sets or perturbations. Future work will evaluate the robustness of 3DSTSRE impacts using different IC/LBC configurations or ensemble-based experimental frameworks. Fourth, it is worth noting that over very high-elevation terrain like TP, the effective sensitivity of upper-level infrared channels may shift downward and become relatively more surface sensitive. In such conditions, improvements in background LST induced by enhanced representation of terrain radiative processes may indirectly affect the BT simulations of these channels through surface-boundary-layer coupling, while substantial atmospheric contributions are still retained. A systematic investigation of whether and how 3DSTSRE influences upper-level infrared BT simulations over very high terrain is therefore challenging and left for future work. Fifth, the current analysis is based on a single summer month (August 2018), during which higher solar elevation angles inherently weaken the terrain shading and aspect-dependent geometric modulation of solar incidence compared with other seasons. Previous multi-season evaluations have shown that the 3DSTSRE impacts on $SW_{\downarrow}$ and LST exhibit clear seasonal dependence, with the most significant relative improvements occurring in winter (Huang et al., 2022; Zhang et al., 2024). It is therefore both valuable and necessary to extend the present framework to other seasons to systematically compare how the improved 3DSTSRE representation mitigates terrain-dependent biases in $SW_{\downarrow}$, LST, and the resulting surface-sensitive infrared BT simulations under contrasting solar geometry conditions. Moreover, other season-specific factors, for example, atmospheric transparency, surface emissivity changes associated with snow cover, and cloud occurrence frequency, should be considered as they may also modulate the propagation of $SW_{\downarrow}$ and LST improvements into BT simulations. Sixth, the clear-sky BT evaluation in this study relies on the FY-4A official cloud mask product (Wang et al., 2019), which has been systematically validated to show high cloud detection accuracy. However, due to the challenging detection of terrain-shadowed and thin cirrus clouds over mountainous regions, some nominally clear-sky samples may therefore contain trace cloud contamination, which could add noise to the OMB statistics and potentially obscure part of the 3DSTSRE signal. Future work could mitigate this limitation by adopting available improved cloud mask products and by extending the study period and spatial domain to increase sample sizes, thereby reducing the stochastic impact of residual cloud contamination through spatiotemporal averaging. Finally, this study employed an offline, static GSI analysis. Implementing a coupled data assimilation system that directly assimilates the improved background fields would be a critical next step to fully quantify their impact on numerical weather prediction skill.

Conflict of Interest

The authors declare no conflicts of interest relevant to this study.

Availability Statement

The East Asia-Pacific surface longwave/shortwave downward radiation data set from 2016 to 2020 (Letu et al., 2022), seamless hourly LST data set with 0.02° resolution over East Asia from 2016 to 2021 (Cheng et al., 2022), and integration data set of Tibetan Plateau boundary (Zhang, 2019) are collected from the National Tibetan Plateau Data Center (https://data.tpdc.ac.cn/en/). The FY-4A/AGRI brightness temperature observation and cloud mask products (Wang et al., 2019; Yang et al., 2017) are obtained from the National Satellite Meteorological Center of China (http://satellite.nsmc.org.cn/). The 3-hr NCEP Global Forecast System real-time forecasts are available at https://rda.ucar.edu/datasets/ds084.1 (NCEP, 2015). The daily real-time global sea surface temperature data set with a 0.5° × 0.5° resolution can be downloaded from ftp://polar.ncep.noaa.gov/pub/history/sst/rtg_high_res (Thiebaux et al., 2003). We acknowledge the use of NCAR Command Language version 6.6.2 (http://dx.doi.org/10.5065/D6WD3XH5) to analyze the model results and plot all the figures.

Acknowledgments
This work was supported by the National Natural Science Foundation of China (42322507), the National Key R & D Program of China (2022YFC3080500), the National Natural Science Foundation of China (42305015, 42275167, 42375157) and the Beijige Research Fund of NJIAS (BJG202403). We thank the anonymous reviewers for their constructive comments that helped us greatly in revising the originally submitted manuscript.

References

Arthur, R. S., Lundquist, K. A., Mirocha, J. D., & Chow, F. K. (2018). Topographic effects on radiation in the WRF model with the immersed boundary method: Implementation, validation, and application to complex terrain. *Monthly Weather Review*, *164*(10), 3277–3292. https://doi.org/10.1175/MWR-D-18-0108.1

Bessho, K., Date, K., Hayashi, M., Ikeda, A., Imai, T., Inoue, H., et al. (2016). An introduction to Himawari-8/9-Japan's new-generation geostationary meteorological satellites. *J. Meteor. Soc. Japan*, *94*(2), 151–183. https://doi.org/10.2151/jmsj.2016-009

Borbas, E. E., & Ruston, B. C. (2010). The RTTOV UWiremis IR land surface emissivity module. Version 1. *NWP SAF Mission Rep. NWPSAF-MO-VS-042*, 24. https://nwpsaf.eu/vs_reports/nwpsaf-mo-vs-042.pdf

Cai, S. X., Huang, A. N., Zhu, K. F., Guo, W. D., Wu, Y., & Gu, C. L. (2023). The forecast skill of the summer precipitation over Tibetan Plateau improved by the adoption of a 3D sub-grid terrain solar radiative effect scheme in a convection-permitting model. *Journal of Geophysical Research*, *128*(11), e2022JD038105. https://doi.org/10.1029/2022JD038105

Cai, S. X., Zhu, K. F., Huang, A. N., Gu, C. L., Wu, Y., Zhu, X. S., & Zhao, W. (2025). Impacts of local and remote sub-grid terrain solar radiative effect on the Meiyu rainfall forecast in the Yangtze-Huaihe River Basin, China. *Journal of Geophysical Research*, *130*(22), e2025JD044324. https://doi.org/10.1029/2025JD044324

Cayla, F.-R. (2001). L'interféromètre IASI, un nouveau sondeur satellitaire à haute résolution. *Meteor. Ser.*, *8*(32), 23–39. https://doi.org/10.4267/2042/36150

Chahine, M. T., Pagano, T. S., Aumann, H. H., Atlas, R., Barnet, C., Blaisdell, J., et al. (2006). AIRS: Improving weather forecasting and providing new data on greenhouse gases. *Bulletin of the American Meteorological Society*, *87*(7), 911–926. https://doi.org/10.1175/BAMS-87-7-911

Chen, Y., Hall, A., & Liou, K.-N. (2006). Application of three-dimensional solar radiative transfer to mountains. *Journal of Geophysical Research*, *111*(D21). https://doi.org/10.1029/2006JD007163

Cheng, J., Dong, S., & Shi, J. (2022). 0.02° seamless hourly land surface temperature dataset over East Asia (2016-2021) [Dataset]. *National Tibetan Plateau/Third Pole Environment Data Center*. https://doi.org/10.11888/Cryos.tpdc.272511

Chu, Q., Yan, G. J., Qi, J. B., Mu, X. H., Li, L. Y., Tong, Y. Y., et al. (2020). Quantitative analysis of terrain reflected solar radiation in snow-covered mountains: A case study in Southeastern Tibetan Plateau. *Journal of Geophysical Research*, *126*(11), e2020JD034294. https://doi.org/10.1029/2020JD034294

Collard, A. D., & McNally, A. P. (2009). The assimilation of infrared atmospheric sounding interferometer radiances at ECMWF. *The Quarterly Journal of the Royal Meteorological Society*, *135*(641), 1044–1058. https://doi.org/10.1002/qj.410

Collins, W. D., Rasch, P. J., Boville, B. A., Hack, J. J., McCaa, J. R., Williamson, D. L., et al. (2004). Description of the NCAR community atmosphere model (CAM 3.0). *NCAR Tech. Note NCAR/TN-464+ STR*, *226*, 1326–1334. https://doi.org/10.5065/D63N21CH

Dong, S. Y., Cheng, J., Shi, J. C., Shi, C. X., Sun, S., & Liu, W. H. (2022). A data fusion method for generating hourly seamless land surface temperature from Himawari-8 AHI data. *Remote Sensing*, *14*(20), 5170. https://doi.org/10.3390/rs14205170

Dozier, J., & Frew, J. (1990). Rapid calculation of terrain parameters for radiation modeling from digital elevation data. *IEEE Transactions on Geoscience and Remote Sensing*, *28*(5), 963–969. https://doi.org/10.1109/36.58986

Dozier, J., & Outcalt, S. I. (1979). An approach toward energy balance simulation over rugged terrain. *Geographical Analysis*, *11*(1), 65–85. https://doi.org/10.1111/j.1538-4632.1979.tb00673.x

Dutta, S. K., Garand, L., & Heilliette, S. (2016). Assimilation of infrared radiance observations with sensitivity to land surfaces in the Canadian ensemble-variational system. *Journal of Atmospheric and Oceanic Technology*, *55*(3), 561–578. https://doi.org/10.1175/JAMC-D-15-0208.1

Dutta, S. K., Garand, L., & Heillietts, S. (2015). Impact evaluation of assimilating surface sensitive infrared radiance observations over land and sea ice from observing system simulation experiments. *Advances in Meteorology*, *2015*(1b). https://doi.org/10.1155/2015/847561

English, S. J. (2008). The importance of accurate skin temperature in assimilating radiances from satellite sounding instruments. *IEEE Transactions on Geoscience and Remote Sensing*, *46*(2), 403–408. https://doi.org/10.1109/TGRS.2007.902413

Fan, X., Gu, Y., Liou, K.-N., Lee, W. L., Zhao, B., Chen, H. B., & Lu, D. (2019). Modeling study of the impact of complex terrain on the surface energy and hydrology over the Tibetan Plateau. *Climate Dynamics*, *53*(11), 6919–6932. https://doi.org/10.1007/s00382-019-04966-z

Gallus, W. A., Jr., & Bresch, J. F. (2006). Comparison of impacts of WRF dynamic core, physics package, and initial conditions on warm season rainfall forecasts. *Monthly Weather Review*, *134*(9), 2632–2641. https://doi.org/10.1175/MWR3198.1

Garand, L., Buehner, M., & Wagneur, N. (2004). Background error correlation between surface skin and air temperatures: Estimation and impact on the assimilation of infrared window radiances. *Journal of Applied Remote Sensing*, *43*(12), 1853–1863. https://doi.org/10.1175/JAM2175.1

Gravelle, C. M., Mecikalski, J. R., Line, W. E., Bedka, K. M., Petersen, R. A., Sieglaff, J. M., et al. (2016). Demonstration of a GOES-R satellite convective toolkit to bridge the gap between severe weather watches and warnings: An example from the 20 May 2013 Moore, Oklahoma, tornado outbreak. *Bulletin of the American Meteorological Society*, *97*(1), 69–84. https://doi.org/10.1175/BAMS-D-14-00054.1

Grell, G. A., & Devenyi, D. (2002). A generalized approach to parameterizing convection combining ensemble and data assimilation techniques. *Geophysical Research Letters*, *29*(14), 1693. https://doi.org/10.1029/2002GL015311

Gu, C. L., Huang, A. N., Li, X., & Wu, Y. (2024a). Offline correction of CMIP6 HighResMIP simulated surface solar irradiance with 3D sub-grid terrain radiative effects. *Geophysical Research Letters*, *51*(10), e2023GL107737. https://doi.org/10.1029/2023GL107737

Gu, C. L., Huang, A. N., Li, X., & Wu, Y. (2024b). The cold bias in the surface air temperature simulations over the Tibetan Plateau of RegCM4 reduced by adopting the 3D sub-grid terrain longwave radiative effect scheme. *Journal of Geophysical Research*, *129*(23), e2024JD042102. https://doi.org/10.1029/2024JD042102

Gu, C. L., Huang, A. N., Li, X., Yang, B., & Wu, Y. (2024). Construction of a clear-sky three dimensional sub-grid terrain longwave radiative effect parameterization scheme under isotropic assumption. *Journal of Geophysical Research*, *129*(4), e2023JD039383. https://doi.org/10.1029/2023JD039383

Gu, C. L., Huang, A. N., Zhang, Y. C., Yang, B., Cai, S. X., Xu, X. K., et al. (2022). The wet bias of RegCM4 over Tibet Plateau in summer reduced by adopting the 3D sub-grid terrain solar radiative effect parameterization scheme. *Journal of Geophysical Research*, *127*(21), e2022JD037434. https://doi.org/10.1029/2022JD037434

Gu, Y., Liou, K.-N., Lee, W. L., & Leung, L. R. (2012). Simulating 3-D radiative transfer effects over the Sierra Nevada Mountains using WRF. *Atmospheric Chemistry and Physics*, *12*(20), 9965–9976. https://doi.org/10.5194/acp-12-9965-2012

Guedj, S., Karbou, F., & Rabier, F. (2011). Land surface temperature estimation to improve the assimilation of SEVIRI radiances over land. *Journal of Geophysical Research*, *116*(D14), D14107. https://doi.org/10.1029/2011JD015776

Han, Y., Weng, F., Liu, Q., & Delst, P. V. (2007). A fast radiative transfer model for SSMIS upper atmosphere sounding channels. *Journal of Geophysical Research*, *112*(D11), D11121. https://doi.org/10.1029/2006JD008208

Hao, D. L., Bisht, G., Gu, Y., Lee, W. L., Liou, K.-N., & Leung, L. R. (2021). A parameterization of sub-grid topographical effects on solar radiation in the E3SM land model (version 1.0): Implementation and evaluation over the Tibetan Plateau. *Geoscientific Model Development*, *14*(10), 6273–6289. https://doi.org/10.5194/gmd-14-6273-2021

Hao, D. L., Bisht, G., Li, L. C., & Leung, L. R. (2025). Representing fine-scale topographic effects on surface radiation balance in hyper-resolution land surface models. *Journal of Advances in Modeling Earth Systems*, *17*(8), e2025MS004987. https://doi.org/10.1029/2025MS004987

Hilton, F., Armante, R., August, T., Barnet, C., Bouchard, A., Camy-Peyret, C., et al. (2012). Hyperspectral earth observation from IASI: Five years of accomplishments. *Bulletin of the American Meteorological Society*, *93*(3), 347–370. https://doi.org/10.1175/BAMS-D-11-00027.1

Hock, R., & Holmgren, B. (2005). A distributed surface energy-balance model for complex topography and its application to Storglaciären, Sweden. *Journal of Glaciology*, *51*(172), 25–36. https://doi.org/10.3189/172756505781829566

Hong, S. Y., & Lim, J. (2006). The WRF single-moment 6-class microphysics scheme (WSM6). *J. Korean Meteorol. Soc.*, *42*, 129–151.

Hong, S. Y., Noh, Y., & Dudhia, J. (2006). A new vertical diffusion package with an explicit treatment of entrainment processes. *Monthly Weather Review*, *134*(9), 2318–2341. https://doi.org/10.1175/MWR3199.1

Hu, M., Ge, G. Q., Shao, H., Stark, D., Newman, K., Zhou, C. H., et al. (2017). *Grid-point statistical interpolation (GSI) User's guide version 3.6*. Developmental Testbed Center. Retrieved from http://www.dtcenter.org/com-GSI/users/docs/index.php.149

Huang, A. N., Gu, C. L., Zhang, Y. C., Li, W. P., Zhang, L. J., Wu, Y., et al. (2022). Development of a clear-sky 3D sub-grid terrain solar radiative effect parameterization scheme based on the mountain radiation theory. *Journal of Geophysical Research*, *127*(13), e2022JD036449. https://doi.org/10.1029/2022JD036449

Hulley, G. C., Hook, S. J., Abbott, E., Malakar, N., Islam, R., & Abrams, M. (2015). The ASTER global emissivity dataset (ASTER GED): Mapping earth's emissivity at 100 meter spatial scale. *Geophysical Research Letters*, *42*(19), 7966–7976. https://doi.org/10.1002/2015GL065564

Ineichen, P. (2008). A broadband simplified version of the solis clear sky model. *Solar Energy*, *82*(8), 758–762. https://doi.org/10.1016/j.solener.2008.02.009

Jarvis, A., Reuter, H. I., Nelson, A., & Guevara, E. (2008). The shuttle radar topography mission (SRTM) 90m digital elevation database v4 [Dataset]. *International Centre for Tropical Agriculture (CIAT)*, *1*. https://developers.google.com/earth-engine/datasets/catalog/CGIAR_SRTM90_V4

Karbou, F., Gérard, E., & Rabier, F. (2010). Global 4DVAR assimilation and forecast experiments using AMSU observations over land. Part I: Impacts of various land surface emissivity parameterizations. *Weather and Forecasting*, *25*(1), 5–19. https://doi.org/10.1175/2009WAF2222243.1

Karlsson, K. G., Anttila, K., Trentmann, J., Stengel, M., Meirink, J. F., Devasthale, A., et al. (2017). CLARA-A2: The second edition of the CM SAF cloud and radiation data record from 34 years of global AVHRR data. *Atmospheric Chemistry and Physics*, *17*(6), 5809–5828. https://doi.org/10.5194/acp-17-5809-2017

Kazumori, M. (2018). Assimilation of Himawari-8 clear sky radiance data in JMA's global and mesoscale NWP systems. *J. Meteor. Soc. Japan*, *96*, 173–192. https://doi.org/10.2151/jmsj.2018-037

Kumar, P., Kishtawal, C. M., & Pal, P. K. (2017). Impact of ECMWF, NCEP, and NCMRWF global model analysis on the WRF model forecast over Indian region. *Theoretical and Applied Climatology*, *127*(1–2), 143–151. https://doi.org/10.1007/s00704-015-1629-1

Lee, W.-L., Gu, Y., Liou, K. N., Leung, L. R., & Hsu, H.-H. (2015). A global model simulation for 3-D radiative transfer impact on surface hydrology over the Sierra Nevada and Rocky Mountains. *Atmospheric Chemistry and Physics*, *15*(10), 5405–5413. https://doi.org/10.5194/acp-15-5405-2015

Lee, W. L., Liou, K.-N., & Hall, A. (2011). Parameterization of solar fluxes over mountain surfaces for application to climate models. *Journal of Geophysical Research*, *116*(D1), D01101. https://doi.org/10.1029/2010jd014722

Lee, W. L., Liou, K.-N., & Wang, C.-c. (2013). Impact of 3-D topography on surface radiation budget over the Tibetan Plateau. *Theoretical and Applied Climatology*, *113*(1–2), 95–103. https://doi.org/10.1007/s00704-012-0767-y

Lee, W. L., Liou, K.-N., Wang, C.-c., Gu, Y., Hsu, H.-H., & Li, J.-L. F. (2019). Impact of 3-D radiation-topography interactions on surface temperature and energy budget over the Tibetan Plateau in winter. *Journal of Geophysical Research*, *124*(3), 1537–1549. https://doi.org/10.1029/2018JD029592

Letu, H., Nakajima, T. Y., Wang, T., Shang, H., Ma, R., Yang, K., et al. (2022). A new benchmark for surface radiation products over the East Asia–Pacific region retrieved from the Himawari-8/AHI next-generation geostationary satellite [Dataset]. *Bulletin of the American Meteorological Society*, *103*(3), E873–E888. https://doi.org/10.1175/BAMS-D-20-0148.1

Li, C. W., Lu, H., Leung, R. L., Yang, K., Li, H. Y., Wang, W., et al. (2019). Improving land surface temperature simulation in CoLM over the Tibetan Plateau through fractional vegetation cover derived from a remotely sensed clumping index and model-simulated leaf area index. *Journal of Geophysical Research*, *124*(5), 2620–2642. https://doi.org/10.1029/2018JD028640

Li, J. D., Miao, C. Y., Wei, W., Zhang, G., Hua, L. J., Chen, Y. L., & Wang, X. (2021). Evaluation of CMIP6 global climate models for simulating land surface energy and water fluxes during 1979-2014. *Journal of Advances in Modeling Earth Systems*, *13*(6), e2021MS002515. https://doi.org/10.1029/2021MS002515

Li, M. S., Liu, X. R., Shu, L., Yin, S. C., Wang, L. Z., Fu, W., et al. (2021). Variations in surface roughness of heterogeneous surfaces in the Nagqu area of the Tibetan Plateau. *Hydrology and Earth System Sciences*, *25*(5), 2915–2930. https://doi.org/10.5194/hess-25-2915-2021

Li, X., Huang, A. N., Zeng, M. J., Wu, Y., Gu, C. L., & Wang, N. (2024). Implementing parameterizations of sub-pixel terrain long-wave radiative effect for FY-4A/AGRI infrared data assimilation over land based on the community radiative transfer model. *Journal of Geophysical Research*, *129*(23), e2024JD042059. https://doi.org/10.1029/2024JD042059

Li, X., Zou, X. L., Zeng, M. J., Zhuge, X. Y., & Liu, W. G. (2023). Improving AHI radiance assimilation over land with the surface skin temperature constrained by station observations and its impact for quantitative precipitation forecasts. *Monthly Weather Review*, *151*(11), 2925–2947. https://doi.org/10.1175/MWR-D-23-0052.1

Li, X., Zou, X. L., Zeng, M. J., Zhuge, X. Y., Wu, Y., & Wang, N. (2024). Surface temperature assimilation improving geostationary meteorological satellite surface-sensitive brightness temperature simulations over land. *Atmospheric Research*, *311*, 107706. https://doi.org/10.1016/j.atmosres.2024.107706

Liang, S. L., Cheng, J., Jia, K., Jiang, B., Liu, Q., Xiao, Z. Q., et al. (2021). The global land surface satellite (GLASS) product suite. *Bulletin of the American Meteorological Society*, *102*(2), E323–E337. https://doi.org/10.1175/BAMS-D-18-0341.1

Liou, K.-N., Gu, Y., Leung, L. R., Lee, W. L., & Fovell, R. G. (2013). A WRF simulation of the impact of 3-D radiative transfer on surface hydrology over the rocky Mountains and Sierra Nevada. *Atmospheric Chemistry and Physics*, *13*(23), 11709–11721. https://doi.org/10.5194/acp-13-11709-2013

Liou, K.-N., Lee, W. L., & Hall, A. (2007). Radiative transfer in mountains: Application to the Tibetan Plateau. *Geophysical Research Letters*, *34*(23). https://doi.org/10.1029/2007GL031762

Lipton, A. E., & Ward, J. M. (1997). Satellite-view biases in retrieved surface temperatures in mountain areas. *Remote Sensing of Environment*, *60*(1), 92–100. https://doi.org/10.1016/S0034-4257(96)00165-4

Liu, S., Li, X., Xu, Z., Che, T., Xiao, Q., Ma, M., et al. (2018). The Heihe integrated observatory network: A basin-scale land surface processes observatory in China. *Vadose Zone Journal*, *17*(1), 1–21. https://doi.org/10.2136/vzj2018.04.0072

Liu, S. M., Li, X., Che, T., Xu, Z. W., Zhang, Y., & Tan, J. L. (2016a). HiWATER: Dataset of hydrometeorological observation network (automatic weather station of A'rou shady slope station, 2014). *A Big Earth Data Platform for Three Poles*. https://doi.org/10.3972/hiwater.250.2015.db

Liu, S. M., Li, X., Che, T., Xu, Z. W., Zhang, Y., & Tan, J. L. (2016b). HiWATER: Dataset of hydrometeorological observation network (automatic weather station of A'rou sunny slope station, 2014). *A Big Earth Data Platform for Three Poles*. https://doi.org/10.3972/hiwater.249.2015.db

Lu, L., Venus, V., Skidmore, A., Wang, T. J., & Luo, G. P. (2011). Estimating land-surface temperature under clouds using MSG/SEVIRI observations. *International Journal of Applied Earth Observation and Geoinformation*, *13*(2), 265–276. https://doi.org/10.1016/j.jag.2010.12.007

Ma, X. G., Jin, J. M., Liu, J., & Niu, G. Y. (2019). An improved vegetation emissivity scheme for land surface modeling and its impact on snow cover simulations. *Climate Dynamics*, *53*(9–10), 6215–6226. https://doi.org/10.1007/s00382-019-04924-9

Ma, Z., Maddy, E. S., Zhang, B., Zhu, T., & Boukabara, S. A. (2017). Impact assessment of Himawari-8 AHI data assimilation in NCEP GDAS/GFS with GSI. *Journal of Atmospheric and Oceanic Technology*, *34*(4), 797–815. https://doi.org/10.1175/JTECH-D-16-0136.1

Manners, J., Vosper, S. B., & Roberts, N. (2012). Radiative transfer over resolved topographic features for high-resolution weather prediction. *Quarterly Journal of the Royal Meteorological Society*, *138*(664), 720–733. https://doi.org/10.1002/qj.956

Martins, J. P. A., Trigo, I. F., Ghilain, N., Jimenez, C., Göttsche, F.-M., Ermida, S. L., et al. (2019). An all-weather land surface temperature product based on MSG/SEVIRI observations. *Remote Sensing*, *11*(24), 3044. https://doi.org/10.3390/rs11243044

McNally, A. P., Watts, P. D., Smith, J. A., Engelen, R., Kelly, G. A., Thépaut, J. N., et al. (2006). The assimilation of AIRS radiance data at ECMWF. *The Quarterly Journal of the Royal Meteorological Society*, *132*(616), 935–957. https://doi.org/10.1256/qj.04.171

Minamide, M., & Zhang, F. (2017). Adaptive observation error inflation for assimilating all-sky satellite radiance. *Monthly Weather Review*, *145*(3), 1063–1081. https://doi.org/10.1175/MWR-D-16-0257.1

Mitchell, K., Mike, E. K., Vince, W., Dag, L., & Paul, R. (2005). The community Noah land-surface model (LSM).

NCEP. (2015). NCEP GFS 0.25° global forecast grids historical archive [Dataset]. Retrieved from https://rda.ucar.edu/datasets/ds084.1/

Okabe, I., & Okamoto, K. (2023). *Assimilation of surface-sensitive bands' clear-sky radiance data using retrieved surface temperatures from geostationary satellites* (pp. 1473–1497). Quarterly Journal of the Royal Meteorological Society. https://doi.org/10.1002/qj.4469

Okamoto, K., Ishibashi, T., & Okabe, I. (2023). All-sky infrared radiance assimilation of a geostationary satellite in the Japan Meteorological Agency's global system. *The Quarterly Journal of the Royal Meteorological Society*, *149*(755), 2477–2503. https://doi.org/10.1002/qj.4516

Ouaknine, J., Gode, S., Napierala, B., Viard, T., Foerster, U., Frar, S., et al. (2013). MTG flexible combined imager optical design and performances. *Proceedings of SPIE - The International Society for Optical Engineering*, (Vol. 8866, pp. 384–397). https://doi.org/10.1117/12.2023078

Pavelin, E. G., & Candy, B. (2014). Assimilation of surface-sensitive infrared radiances over land: Estimation of land surface temperature and emissivity. *The Quarterly Journal of the Royal Meteorological Society*, *140*(681), 1198–1208. https://doi.org/10.1002/qj.2218

Proy, C., Tanré, D., & Deschamps, P. Y. (1989). Evaluation of topographic effects in remotely sensed data. *Remote Sensing of Environment*, *30*(1), 21–32. https://doi.org/10.1016/0034-4257(89)90044-8

Robledano, A., Picard, G., Arnaud, L., Larue, F., & Ollivier, I. (2022). Modelling surface temperature and radiation budget of snow-covered complex terrain. *The Cryosphere*, *16*(2), 559–579. https://doi.org/10.5194/tc-16-559-2022

Schmetz, J., Pili, P., Tjemkes, S., Just, D., Kerkmann, J., Rota, S., & Ratier, A. (2002). An introduction to meteosat second generation (MSG). *Bulletin of the American Meteorological Society*, *83*(7), 977–992. https://doi.org/10.1175/1520-0477(2002)083<0977:AITMSG>2.3.CO;2

Schmit, T. J., Griffith, P., Gunshor, M. M., Daniels, J. M., Goodman, S. J., & Lebair, W. J. (2017). A closer look at the ABI on the GOES-R series. *Bulletin of the American Meteorological Society*, *98*(4), 681–698. https://doi.org/10.1175/BAMS-D-15-00230.1

Schmit, T. J., Gunshor, M. M., Menzel, P. W., Gurka, J. J., Li, J., & Bachmeier, A. S. (2005). Introducing the next-generation advanced baseline imager (ABI) on geostationary operational environmental satellites (GOES)-R. *Bulletin of the American Meteorological Society*, *86*(8), 1079–1096. https://doi.org/10.1175/BAMS-86-8-1079

Seemann, S. W., Borbas, E. E., Knuteson, R. O., Stephenson, R. G., & Huang, H. L. (2007). Development of a global infrared emissivity database for application to clear sky sounding retrieval from multispectral satellite radiances measurements. *Journal of Applied Meteorology and Climatology*, *47*(1), 108–123. https://doi.org/10.1175/2007JAMC1590.1

Sharpnack, D. A., & Akin, G. (1969). An algorithm for computing slope and aspect from elevations. *Photogrammetric Engineering*, *35*(3), 247–248.

Shepard, D. (1968). A two-dimensional interpolation function for irregularly-spaced data. In *Proceedings of the 1968 ACM National Conference, 27-29 August 1968* (pp. 517–524). https://doi.org/10.1145/800186.810616

Skamarock, C., Klemp, B., Dudhia, J., Gill, O., Liu, Z. Q., Berner, J., et al. (2019). A description of the advanced research WRF model version 4. https://doi.org/10.5065/1DFH-6P97

Skidmore, A. K. (1989). A comparison of techniques for calculating gradient and aspect from a gridded digital elevation model. *International Journal of Geographical Information Systems*, *3*(4), 323–334. https://doi.org/10.1080/02693798908941519

Stengel, M., Undén, P., Lindskog, M., Dahlgren, P., Gustafsson, N., & Bennartz, R. (2009). Assimilation of SEVIRI infrared radiances with HIRLAM 4D-Var. Quart. *J. Roy. Meteor. Soc.*, *135*(645), 2100–2109. https://doi.org/10.1002/qj.501

Thiebaux, J., Rogers, E., Wang, W. Q., & Katz, B. (2003). A new high-resolution blended real-time global sea surface temperature analysis. *Bulletin of the American Meteorological Society*, *84*(5), 645–656. https://doi.org/10.1175/BAMS-84-5-645

Tian, Y. Q., Davies-Colley, R. J., Gong, P., & Thorrold, B. W. (2001). Estimating solar radiation on slopes of arbitrary aspect. *Agric. For. Meteor.*, *109*(1), 67–74. https://doi.org/10.1016/S0168-1923(01)00245-3

Toth, Z., & Kalnay, E. (1993). Ensemble forecasting at NMC: The generation of perturbations. *Bulletin of the American Meteorological Society*, *74*(12), 2317–2330. https://doi.org/10.1175/1520-0477(1993)074<2317:EFANTG>2.0.CO;2

Tovar, J., Olmo, F. J., & Alados-Arboledas, L. (1995). Local scale variability of solar radiation in a mountainous region. *Journal of Applied Meteorology*, *34*(10), 2316–2322. https://doi.org/10.1175/1520-0450(1995)034<2316:LSVOSR>2.0.CO;2

Trigo, I. F., Boussetta, S., Viterbo, P., Balsamo, G., & Sandu, I. (2015). Comparison of model land skin temperature with remotely sensed estimates and assessment of surface atmosphere coupling. *Journal of Geophysical Research*, *120*(23), 12096–12111. https://doi.org/10.1002/2015JD023812

Vogel, R. L., Liu, Q. H., Han, Y., & Weng, F. Z. (2011). Evaluating a satellite-derived global infrared land surface emissivity data set for use in radiative transfer modeling. *Journal of Geophysical Research*, *116*(D8), D08105. https://doi.org/10.1029/2010JD014679

Wang, T. X., Yan, G. J., Mu, X. H., Jiao, Z. H., Chen, L., & Chu, Q. (2018). Toward operational shortwave radiation modeling and retrieval over rugged terrain. *Remote Sensing of Environment*, *205*, 419–433. https://doi.org/10.1016/j.rse.2017.11.006

Wang, X., Min, M., Wang, F., Guo, J., Li, B., & Tang, S. (2019). Intercomparisons of cloud mask products among Fengyun-4A, Himawari-8, and MODIS. *IEEE Transactions on Geoscience and Remote Sensing*, *57*(11), 8827–8839. https://doi.org/10.1109/TGRS.2019.2923247

Wu, Y., Huang, A. N., Yang, B., Dong, G. T., Wen, L. J., Lazhu, et al. (2019). Numerical study on the climatic effect of the lake clusters over Tibetan Plateau in summer. *Climate Dynamics*, *53*(9–10), 5215–5236. https://doi.org/10.1007/s00382-019-04856-4

Xu, L., Cheng, W., Deng, Z. R., Liu, J. J., Wang, B., Liu, B., et al. (2023). Assimilation of the FY-4A AGRI clear-sky radiance data in a regional numerical model and its impact on the forecast of the 21·7 Henan extremely persistent heavy rainfall. *Advances in Atmospheric Sciences*, *40*(5), 920–936. https://doi.org/10.1007/s00376-022-1380-3

Yan, G. J., Jiao, Z. H., Wang, T. X., & Mu, X. H. (2020). Modeling surface longwave radiation over high-relief terrain. *Remote Sensing of Environment*, *237*, 111556. https://doi.org/10.1016/j.rse.2019.111556

Yan, G. J., Wang, T. X., Jiao, Z. H., Mu, X. H., Zhao, J., & Chen, L. (2016). Topographic radiation modeling and spatial scaling of clear-sky land surface longwave radiation over rugged terrain. *Remote Sensing of Environment*, *172*, 15–27. https://doi.org/10.1016/j.rse.2015.10.026

Yang, J., Zhang, Z., Wei, C., Lu, F., & Guo, Q. (2017). Introducing the new generation of Chinese geostationary weather satellites, Fengyun-4. *Bulletin of the American Meteorological Society*, *98*(8), 1637–1658. https://doi.org/10.1175/BAMS-D-16-0065.1

Zhang, X. D., Huang, A. N., Dai, Y. J., Li, W. P., Gu, C. L., Yuan, H., et al. (2022). Influences of 3D sub-grid terrain radiative effect on the performance of CoLM over Heihe River Basin, Tibetan Plateau. *Journal of Advances in Modeling Earth Systems*, *14*(1), e2021MS002654. https://doi.org/10.1029/2021MS002654

Zhang, X. D., Huang, A. N., Yang, X. Y., Gu, C. L., Cai, S. X., & Luo, J. X. (2024). Performance of common land model in simulating the land surface thermal and hydrological processes over China improved by including the sub-grid terrain solar radiative effect. *Journal of Geophysical Research*, *129*(24), e2023JD039775. https://doi.org/10.1029/2023JD039775

Zhang, Y. L. (2019). Integration dataset of Tibet Plateau boundary [Dataset]. *National Tibetan Plateau/Third Pole Environment Data Center*. https://doi.org/10.11888/Geogra.tpdc.270099

Zheng, W. Z., Wei, H. L., Wang, Z., Zeng, X. B., Meng, J., Ek, M., et al. (2012). Improvement of daytime land surface skin temperature over arid regions in the NCEP GFS model and its impact on satellite data assimilation. *Journal of Geophysical Research*, *117*(D6), D06117. https://doi.org/10.1029/2011JD015901

Zhou, S. G., & Cheng, J. (2020). An improved temperature and emissivity separation algorithm for the advanced Himawari imager. *IEEE Transactions on Geoscience and Remote Sensing*, *58*(10), 7105–7123. https://doi.org/10.1109/TGRS.2020.2979846

Zhou, X., Yang, K., Jiang, Y. Z., Sun, J., Chen, Y. Y., Li, X., et al. (2022). The influence of bare ground thermal roughness length parameterization on the simulation of near-surface air and skin temperatures over the Tibetan Plateau. *Journal of Geophysical Research*, *127*(21), e2022JD037245. https://doi.org/10.1029/2022JD037245

Zhuge, X. Y., Zou, X. L., Weng, F. Z., & Sun, M. (2018). Dependence of simulation biases at AHI surface-sensitive channels on land surface emissivity over China. *Journal of Atmospheric and Oceanic Technology*, *35*(6), 1283–1298. https://doi.org/10.1175/JTECH-D-17-0152.1

Zou, X. L., Qin, Z. K., & Weng, F. Z. (2011). Improved coastal precipitation forecasts with direct assimilation of GOES-11/12 imager radiances. *Monthly Weather Review*, *139*(12), 3711–3729. https://doi.org/10.1175/MWR-D-10-05040.1